

# Measurement of Single Muons at Forward Rapidity in $p + p$ Collisions at $\sqrt{s} = 200$ GeV and Implications for Charm Production

S.S. Adler,<sup>5</sup> S. Afanasiev,<sup>17</sup> C. Aidala,<sup>5</sup> N.N. Ajitanand,<sup>43</sup> Y. Akiba,<sup>20,38</sup> J. Alexander,<sup>43</sup> R. Amirikas,<sup>12</sup> L. Aphecetche,<sup>45</sup> S.H. Aronson,<sup>5</sup> R. Auerbeck,<sup>44</sup> T.C. Awes,<sup>35</sup> R. Azmoun,<sup>44</sup> V. Babintsev,<sup>15</sup> A. Baldisseri,<sup>10</sup> K.N. Barish,<sup>6</sup> P.D. Barnes,<sup>27</sup> B. Bassalleck,<sup>33</sup> S. Bathe,<sup>30</sup> S. Batsouli,<sup>9</sup> V. Baublis,<sup>37</sup> A. Bazilevsky,<sup>39,15</sup> S. Belikov,<sup>16,15</sup> Y. Berdnikov,<sup>40</sup> S. Bhagavatula,<sup>16</sup> J.G. Boissevain,<sup>27</sup> H. Borel,<sup>10</sup> S. Borenstein,<sup>25</sup> M.L. Brooks,<sup>27</sup> D.S. Brown,<sup>34</sup> N. Bruner,<sup>33</sup> D. Bucher,<sup>30</sup> H. Buesching,<sup>30</sup> V. Bumazhnov,<sup>15</sup> G. Bunce,<sup>5,39</sup> J.M. Burward-Hoy,<sup>26,44</sup> S. Butsyk,<sup>44</sup> X. Camard,<sup>45</sup> J.-S. Chai,<sup>18</sup> P. Chand,<sup>4</sup> W.C. Chang,<sup>2</sup> S. Chernichenko,<sup>15</sup> C.Y. Chi,<sup>9</sup> J. Chiba,<sup>20</sup> M. Chiu,<sup>9</sup> I.J. Choi,<sup>52</sup> J. Choi,<sup>19</sup> R.K. Choudhury,<sup>4</sup> T. Chujo,<sup>5</sup> V. Cianciolo,<sup>35</sup> Y. Cobigo,<sup>10</sup> B.A. Cole,<sup>9</sup> P. Constantin,<sup>16</sup> D. d'Enterria,<sup>45</sup> G. David,<sup>5</sup> H. Delagrangé,<sup>45</sup> A. Denisov,<sup>15</sup> A. Deshpande,<sup>39</sup> E.J. Desmond,<sup>5</sup> A. Devismes,<sup>44</sup> O. Dietzsch,<sup>41</sup> O. Drapier,<sup>25</sup> A. Drees,<sup>44</sup> K.A. Drees,<sup>5</sup> A. Durum,<sup>15</sup> D. Dutta,<sup>4</sup> Y.V. Efremenko,<sup>35</sup> K. El Chenawi,<sup>49</sup> A. Enokizono,<sup>14</sup> H. En'yo,<sup>38,39</sup> S. Esumi,<sup>48</sup> L. Ewell,<sup>5</sup> D.E. Fields,<sup>33,39</sup> F. Fleuret,<sup>25</sup> S.L. Fokin,<sup>23</sup> B.D. Fox,<sup>39</sup> Z. Fraenkel,<sup>51</sup> J.E. Frantz,<sup>9</sup> A. Franz,<sup>5</sup> A.D. Frawley,<sup>12</sup> S.-Y. Fung,<sup>6</sup> S. Garpman,<sup>29,\*</sup> T.K. Ghosh,<sup>49</sup> A. Glenn,<sup>46</sup> G. Gogiberidze,<sup>46</sup> M. Gonin,<sup>25</sup> J. Gosset,<sup>10</sup> Y. Goto,<sup>39</sup> R. Granier de Cassagnac,<sup>25</sup> N. Grau,<sup>16</sup> S.V. Greene,<sup>49</sup> M. Grosse Perdekamp,<sup>39</sup> W. Guryn,<sup>5</sup> H.-Å. Gustafsson,<sup>29</sup> T. Hachiya,<sup>14</sup> J.S. Haggerty,<sup>5</sup> H. Hamagaki,<sup>8</sup> A.G. Hansen,<sup>27</sup> E.P. Hartouni,<sup>26</sup> M. Harvey,<sup>5</sup> R. Hayano,<sup>8</sup> N. Hayashi,<sup>38</sup> X. He,<sup>13</sup> M. Heffner,<sup>26</sup> T.K. Hemmick,<sup>44</sup> J.M. Heuser,<sup>44</sup> M. Hibino,<sup>50</sup> J.C. Hill,<sup>16</sup> W. Holzmann,<sup>43</sup> K. Homma,<sup>14</sup> B. Hong,<sup>22</sup> A. Hoover,<sup>34</sup> D. Hornback,<sup>46</sup> T. Ichihara,<sup>38,39</sup> V.V. Ikonnikov,<sup>23</sup> K. Imai,<sup>24,38</sup> D. Isenhower,<sup>1</sup> M. Ishihara,<sup>38</sup> M. Issah,<sup>43</sup> A. Isupov,<sup>17</sup> B.V. Jacak,<sup>44</sup> W.Y. Jang,<sup>22</sup> Y. Jeong,<sup>19</sup> J. Jia,<sup>44</sup> O. Jinnouchi,<sup>38</sup> B.M. Johnson,<sup>5</sup> S.C. Johnson,<sup>26</sup> K.S. Joo,<sup>31</sup> D. Jouan,<sup>36</sup> S. Kametani,<sup>8,50</sup> N. Kamihara,<sup>47,38</sup> J.H. Kang,<sup>52</sup> S.S. Kapoor,<sup>4</sup> K. Katou,<sup>50</sup> S. Kelly,<sup>9</sup> B. Khachaturov,<sup>51</sup> A. Khanzadeev,<sup>37</sup> J. Kikuchi,<sup>50</sup> D.H. Kim,<sup>31</sup> D.J. Kim,<sup>52</sup> D.W. Kim,<sup>19</sup> E. Kim,<sup>42</sup> G.-B. Kim,<sup>25</sup> H.J. Kim,<sup>52</sup> E. Kistenev,<sup>5</sup> A. Kiyomichi,<sup>48</sup> K. Kiyoyama,<sup>32</sup> C. Klein-Boesing,<sup>30</sup> H. Kobayashi,<sup>38,39</sup> L. Kochenda,<sup>37</sup> V. Kochetkov,<sup>15</sup> D. Koehler,<sup>33</sup> T. Kohama,<sup>14</sup> M. Kopytine,<sup>44</sup> D. Kotchetkov,<sup>6</sup> A. Kozlov,<sup>51</sup> P.J. Kroon,<sup>5</sup> C.H. Kuberg,<sup>1,27,\*</sup> K. Kurita,<sup>39</sup> Y. Kuroki,<sup>48</sup> M.J. Kweon,<sup>22</sup> Y. Kwon,<sup>52</sup> G.S. Kyle,<sup>34</sup> R. Lacey,<sup>43</sup> V. Ladygin,<sup>17</sup> J.G. Lajoie,<sup>16</sup> A. Lebedev,<sup>16,23</sup> S. Leckey,<sup>44</sup> D.M. Lee,<sup>27</sup> S. Lee,<sup>19</sup> M.J. Leitch,<sup>27</sup> X.H. Li,<sup>6</sup> H. Lim,<sup>42</sup> A. Litvinenko,<sup>17</sup> M.X. Liu,<sup>27</sup> Y. Liu,<sup>36</sup> C.F. Maguire,<sup>49</sup> Y.I. Makdisi,<sup>5</sup> A. Malakhov,<sup>17</sup> V.I. Manko,<sup>23</sup> Y. Mao,<sup>7,38</sup> G. Martinez,<sup>45</sup> M.D. Marx,<sup>44</sup> H. Masui,<sup>48</sup> F. Matathias,<sup>44</sup> T. Matsumoto,<sup>8,50</sup> P.L. McGaughey,<sup>27</sup> E. Melnikov,<sup>15</sup> F. Messer,<sup>44</sup> Y. Miake,<sup>48</sup> J. Milan,<sup>43</sup> T.E. Miller,<sup>49</sup> A. Milov,<sup>44,51</sup> S. Mioduszewski,<sup>5</sup> R.E. Mischke,<sup>27</sup> G.C. Mishra,<sup>13</sup> J.T. Mitchell,<sup>5</sup> A.K. Mohanty,<sup>4</sup> D.P. Morrison,<sup>5</sup> J.M. Moss,<sup>27</sup> F. Mühlbacher,<sup>44</sup> D. Mukhopadhyay,<sup>51</sup> M. Muniruzzaman,<sup>6</sup> J. Murata,<sup>38,39</sup> S. Nagamiya,<sup>20</sup> J.L. Nagle,<sup>9</sup> T. Nakamura,<sup>14</sup> B.K. Nandi,<sup>6</sup> M. Nara,<sup>48</sup> J. Newby,<sup>46</sup> P. Nilsson,<sup>29</sup> A.S. Nyanin,<sup>23</sup> J. Nystrand,<sup>29</sup> E. O'Brien,<sup>5</sup> C.A. Ogilvie,<sup>16</sup> H. Ohnishi,<sup>5,38</sup> I.D. Ojha,<sup>49,3</sup> K. Okada,<sup>38</sup> M. Ono,<sup>48</sup> V. Onuchin,<sup>15</sup> A. Oskarsson,<sup>29</sup> I. Otterlund,<sup>29</sup> K. Oyama,<sup>8</sup> K. Ozawa,<sup>8</sup> D. Pal,<sup>51</sup> A.P.T. Palounek,<sup>27</sup> V. Pantuev,<sup>44</sup> V. Papavassiliou,<sup>34</sup> J. Park,<sup>42</sup> A. Parmar,<sup>33</sup> S.F. Pate,<sup>34</sup> T. Peitzmann,<sup>30</sup> J.-C. Peng,<sup>27</sup> V. Peresedov,<sup>17</sup> C. Pinkenburg,<sup>5</sup> R.P. Pisani,<sup>5</sup> F. Plasil,<sup>35</sup> M.L. Purschke,<sup>5</sup> A.K. Purwar,<sup>44</sup> J. Rak,<sup>16</sup> I. Ravinovich,<sup>51</sup> K.F. Read,<sup>35,46</sup> M. Reuter,<sup>44</sup> K. Reygers,<sup>30</sup> V. Riabov,<sup>37,40</sup> Y. Riabov,<sup>37</sup> G. Roche,<sup>28</sup> A. Romana,<sup>25,\*</sup> M. Rosati,<sup>16</sup> P. Rosnet,<sup>28</sup> S.S. Ryu,<sup>52</sup> M.E. Sadler,<sup>1</sup> N. Saito,<sup>38,39</sup> T. Sakaguchi,<sup>8,50</sup> M. Sakai,<sup>32</sup> S. Sakai,<sup>48</sup> V. Samsonov,<sup>37</sup> L. Sanfratello,<sup>33</sup> R. Santo,<sup>30</sup> H.D. Sato,<sup>24,38</sup> S. Sato,<sup>5,48</sup> S. Sawada,<sup>20</sup> Y. Schutz,<sup>45</sup> V. Semenov,<sup>15</sup> R. Seto,<sup>6</sup> M.R. Shaw,<sup>1,27</sup> T.K. Shea,<sup>5</sup> T.-A. Shibata,<sup>47,38</sup> K. Shigaki,<sup>14,20</sup> T. Shiina,<sup>27</sup> C.L. Silva,<sup>41</sup> D. Silvermyr,<sup>27,29</sup> K.S. Sim,<sup>22</sup> C.P. Singh,<sup>3</sup> V. Singh,<sup>3</sup> M. Sivertz,<sup>5</sup> A. Soldatov,<sup>15</sup> R.A. Soltz,<sup>26</sup> W.E. Sondheim,<sup>27</sup> S.P. Sorensen,<sup>46</sup> I.V. Sourikova,<sup>5</sup> F. Staley,<sup>10</sup> P.W. Stankus,<sup>35</sup> E. Stenlund,<sup>29</sup> M. Stepanov,<sup>34</sup> A. Ster,<sup>21</sup> S.P. Stoll,<sup>5</sup> T. Sugitate,<sup>14</sup> J.P. Sullivan,<sup>27</sup> E.M. Takagui,<sup>41</sup> A. Taketani,<sup>38,39</sup> M. Tamai,<sup>50</sup> K.H. Tanaka,<sup>20</sup> Y. Tanaka,<sup>32</sup> K. Tanida,<sup>38</sup> M.J. Tannenbaum,<sup>5</sup> P. Tarján,<sup>11</sup> J.D. Tepe,<sup>1,27</sup> T.L. Thomas,<sup>33</sup> J. Tojo,<sup>24,38</sup> H. Torii,<sup>24,38</sup> R.S. Towell,<sup>1</sup> I. Tserruya,<sup>51</sup> H. Tsuruoka,<sup>48</sup> S.K. Tuli,<sup>3</sup> H. Tydesjö,<sup>29</sup> N. Tyurin,<sup>15</sup> J. Velkovska,<sup>5,44</sup> M. Velkovsky,<sup>44</sup> V. Veszprémi,<sup>11</sup> L. Villatte,<sup>46</sup> A.A. Vinogradov,<sup>23</sup> M.A. Volkov,<sup>23</sup> E. Vznuzdaev,<sup>37</sup> X.R. Wang,<sup>13</sup> Y. Watanabe,<sup>38,39</sup> S.N. White,<sup>5</sup> F.K. Wohn,<sup>16</sup> C.L. Woody,<sup>5</sup> W. Xie,<sup>6</sup> Y. Yang,<sup>7</sup> A. Yanovich,<sup>15</sup> S. Yokkaichi,<sup>38,39</sup> G.R. Young,<sup>35</sup> I.E. Yushmanov,<sup>23</sup> W.A. Zajc,<sup>9,†</sup> C. Zhang,<sup>9</sup> S. Zhou,<sup>7</sup> S.J. Zhou,<sup>51</sup> L. Zolin,<sup>17</sup> R. duRietz,<sup>29</sup> and H.W. vanHecke<sup>27</sup>

(PHENIX Collaboration)

<sup>1</sup>Abilene Christian University, Abilene, TX 79699, USA

<sup>2</sup>Institute of Physics, Academia Sinica, Taipei 11529, Taiwan

<sup>3</sup>Department of Physics, Banaras Hindu University, Varanasi 221005, India

<sup>4</sup>Bhabha Atomic Research Centre, Bombay 400 085, India

<sup>5</sup>Brookhaven National Laboratory, Upton, NY 11973-5000, USA

<sup>6</sup>University of California - Riverside, Riverside, CA 92521, USA

- <sup>7</sup>China Institute of Atomic Energy (CIAE), Beijing, People's Republic of China
- <sup>8</sup>Center for Nuclear Study, Graduate School of Science, University of Tokyo, 7-3-1 Hongo, Bunkyo, Tokyo 113-0033, Japan
- <sup>9</sup>Columbia University, New York, NY 10027 and Nevis Laboratories, Irvington, NY 10533, USA
- <sup>10</sup>Dapnia, CEA Saclay, F-91191, Gif-sur-Yvette, France
- <sup>11</sup>Debrecen University, H-4010 Debrecen, Egyetem tér 1, Hungary
- <sup>12</sup>Florida State University, Tallahassee, FL 32306, USA
- <sup>13</sup>Georgia State University, Atlanta, GA 30303, USA
- <sup>14</sup>Hiroshima University, Kagamiyama, Higashi-Hiroshima 739-8526, Japan
- <sup>15</sup>Institute for High Energy Physics (IHEP), Protvino, Russia
- <sup>16</sup>Iowa State University, Ames, IA 50011, USA
- <sup>17</sup>Joint Institute for Nuclear Research, 141980 Dubna, Moscow Region, Russia
- <sup>18</sup>KAERI, Cyclotron Application Laboratory, Seoul, South Korea
- <sup>19</sup>Kangnung National University, Kangnung 210-702, South Korea
- <sup>20</sup>KEK, High Energy Accelerator Research Organization, Tsukuba-shi, Ibaraki-ken 305-0801, Japan
- <sup>21</sup>KFKI Research Institute for Particle and Nuclear Physics (RMKI), H-1525 Budapest 114, POBox 49, Hungary
- <sup>22</sup>Korea University, Seoul, 136-701, Korea
- <sup>23</sup>Russian Research Center "Kurchatov Institute", Moscow, Russia
- <sup>24</sup>Kyoto University, Kyoto 606-8502, Japan
- <sup>25</sup>Laboratoire Leprince-Ringuet, Ecole Polytechnique, CNRS-IN2P3, Route de Saclay, F-91128, Palaiseau, France
- <sup>26</sup>Lawrence Livermore National Laboratory, Livermore, CA 94550, USA
- <sup>27</sup>Los Alamos National Laboratory, Los Alamos, NM 87545, USA
- <sup>28</sup>LPC, Université Blaise Pascal, CNRS-IN2P3, Clermont-Fd, 63177 Aubiere Cedex, France
- <sup>29</sup>Department of Physics, Lund University, Box 118, SE-221 00 Lund, Sweden
- <sup>30</sup>Institut für Kernphysik, University of Muenster, D-48149 Muenster, Germany
- <sup>31</sup>Myongji University, Yongin, Kyonggido 449-728, Korea
- <sup>32</sup>Nagasaki Institute of Applied Science, Nagasaki-shi, Nagasaki 851-0193, Japan
- <sup>33</sup>University of New Mexico, Albuquerque, NM 87131, USA
- <sup>34</sup>New Mexico State University, Las Cruces, NM 88003, USA
- <sup>35</sup>Oak Ridge National Laboratory, Oak Ridge, TN 37831, USA
- <sup>36</sup>IPN-Orsay, Université Paris Sud, CNRS-IN2P3, BP1, F-91406, Orsay, France
- <sup>37</sup>PNPI, Petersburg Nuclear Physics Institute, Gatchina, Russia
- <sup>38</sup>RIKEN (The Institute of Physical and Chemical Research), Wako, Saitama 351-0198, JAPAN
- <sup>39</sup>RIKEN BNL Research Center, Brookhaven National Laboratory, Upton, NY 11973-5000, USA
- <sup>40</sup>St. Petersburg State Technical University, St. Petersburg, Russia
- <sup>41</sup>Universidade de São Paulo, Instituto de Física, Caixa Postal 66318, São Paulo CEP05315-970, Brazil
- <sup>42</sup>System Electronics Laboratory, Seoul National University, Seoul, South Korea
- <sup>43</sup>Chemistry Department, Stony Brook University, SUNY, Stony Brook, NY 11794-3400, USA
- <sup>44</sup>Department of Physics and Astronomy, Stony Brook University, SUNY, Stony Brook, NY 11794, USA
- <sup>45</sup>SUBATECH (Ecole des Mines de Nantes, CNRS-IN2P3, Université de Nantes) BP 20722 - 44307, Nantes, France
- <sup>46</sup>University of Tennessee, Knoxville, TN 37996, USA
- <sup>47</sup>Department of Physics, Tokyo Institute of Technology, Tokyo, 152-8551, Japan
- <sup>48</sup>Institute of Physics, University of Tsukuba, Tsukuba, Ibaraki 305, Japan
- <sup>49</sup>Vanderbilt University, Nashville, TN 37235, USA
- <sup>50</sup>Waseda University, Advanced Research Institute for Science and Engineering, 17 Kikui-cho, Shinjuku-ku, Tokyo 162-0044, Japan
- <sup>51</sup>Weizmann Institute, Rehovot 76100, Israel
- <sup>52</sup>Yonsei University, IPAP, Seoul 120-749, Korea
- (Dated: July 30, 2018)

Muon production at forward rapidity ( $1.5 \leq |\eta| \leq 1.8$ ) has been measured by the PHENIX experiment over the transverse momentum range  $1 \leq p_T \leq 3$  GeV/c in  $\sqrt{s} = 200$  GeV  $p+p$  collisions at the Relativistic Heavy Ion Collider. After statistically subtracting contributions from light hadron decays an excess remains which is attributed to the semileptonic decays of hadrons carrying heavy flavor, *i.e.* charm quarks or, at high  $p_T$ , bottom quarks. The resulting muon spectrum from heavy flavor decays is compared to PYTHIA and a next-to-leading order perturbative QCD calculation. PYTHIA is used to determine the charm quark spectrum that would produce the observed muon excess. The corresponding differential cross section for charm quark production at forward rapidity is determined to be  $d\sigma_{c\bar{c}}/dy|_{y=1.6} = 0.243 \pm 0.013(\text{stat.}) \pm 0.105(\text{data syst.})^{+0.049}_{-0.087}(\text{PYTHIA syst.})$  mb.

PACS numbers: 13.85.Qk, 13.20.Fc, 13.20.He, 25.75.Dw

---

\*Deceased

---

†PHENIX Spokesperson: zajc@nevis.columbia.edu

## I. INTRODUCTION

Measurements of heavy quark production in proton-proton ( $p + p$ ) interactions at collider energies serve as important tests for perturbative Quantum ChromoDynamics (pQCD). Bottom production at the Tevatron collider ( $\sqrt{s} = 1.8$  and  $1.96$  TeV/c) [1, 2] is reasonably well described by a recent Fixed Order Next-to-Leading Logarithm (FONLL) calculation [3, 4, 5]. Charm production at FNAL, which has only been measured at relatively high  $p_T$  ( $> 5$  GeV/c), is  $\approx 50\%$  higher than the FONLL prediction [6]. However, theoretical and experimental uncertainties are large, such that significant disagreement between theory and data cannot be claimed.

Measurements at Brookhaven National Laboratory's Relativistic Heavy Ion Collider (RHIC), by both the PHENIX and STAR experiments, have provided a wealth of information on mid-rapidity open charm production in collisions at  $\sqrt{s_{NN}} = 130$  GeV ( $p + p$ ) and  $\sqrt{s_{NN}} = 200$  GeV ( $p + p$ ,  $d + Au$ , and  $Au + Au$ ) down to  $p_T \approx 0.5$  GeV/c. Semileptonic decay of produced charm quarks is the primary source of high  $p_T$  leptons after contributions from known (light hadron) sources are subtracted. Both PHENIX [7, 8, 9, 10, 11, 12, 13, 14, 15, 16] and STAR [17, 18] have made statistical measurements of charm production via single-electron spectra. STAR has also made a direct measurement of charm production through reconstruction of hadronic decay modes of  $D$  mesons [17]. In  $p + p$  collisions at  $\sqrt{s_{NN}} = 200$  GeV PHENIX finds  $d\sigma_{c\bar{c}}/dy|_{y=0} = 0.123 \pm 0.012(\text{stat.}) \pm 0.045(\text{syst.})$  mb [13]. STAR finds a somewhat higher central value,  $d\sigma_{c\bar{c}}/dy|_{y=0} = 0.30 \pm 0.04(\text{stat.}) \pm 0.09(\text{syst.})$  mb [17], but the two measurements are consistent within the stated errors. Both measurements are noticeably (2-4 $\times$ ) higher than PYTHIA (a leading order pQCD event generator) [19, see experimental references for specific parameter sets] and FONLL [20]. Again, quantitative disagreement cannot be established with current experimental and theoretical errors. However, we note that there is some debate about whether charm quarks are heavy enough to be reliably treated by pQCD [21].

Such measurements also serve as an important baseline for charm production in proton-nucleus or deuteron-nucleus ( $p + A$  or  $d + A$ ), and nucleus-nucleus ( $A + B$ ) collisions [22, 23, 24, 25]. In the absence of any nuclear effects, charm production (since it is a point-like process) is expected to scale with the number of binary nucleon-nucleon collisions ( $N_{coll}$ ), which depends on the impact parameter of the nuclear collision and can be obtained from a Glauber calculation [26]. The degree of scaling for any given centrality bin is quantified by the nuclear modification factor:

$$R_{AB} = \frac{1}{N_{coll}^{AB}} \times \frac{dN^{AB}/dy}{dN^{pp}/dy}. \quad (1)$$

Deviations from this scaling ( $R_{AB} \neq 1$ ) in  $p + A$  or  $d + A$  collisions quantify cold nuclear matter effects (such as initial state energy loss [27, 28, 29, 30, 31, 32], and shadowing [33, 34, 35, 36, 37]). Any such deviation must be understood so that in  $A + B$  collisions contributions to  $R_{AB} \neq 1$  from hot nuclear matter effects (such as in-medium energy loss [38, and references therein]) and cold nuclear matter effects can be disentangled. In  $d + Au$  collisions both PHENIX and STAR find little or no effect of cold nuclear matter on charm production ( $R_{dAu} \approx 1$  over the measured lepton  $p_T$  [10, 17]). This contrasts with measurements of open charm in  $Au + Au$  collisions: although the *total* charm production appears to scale with  $N_{coll}$  [8], there is a strong suppression of lepton spectra for  $p_T > 2$  GeV/c that increases with centrality [11, 12, 18]. Furthermore the elliptical flow of non-photonic single electrons, as measured by PHENIX in  $Au + Au$  collisions [14, 15, 16], implies that the charm quarks interact strongly with the created medium.

Finally, since the initial formation of open and closed charm are both sensitive to initial gluon densities [39, 40], open charm production serves as an appropriate normalization for  $J/\psi$  production. The production of  $J/\psi$  mesons is expected to be sensitive to the production of a quark gluon plasma (QGP), should one be formed in  $A + B$  collisions [41, 42, 43, 44, 45, 46]. In order to understand  $J/\psi$  production differences in  $A + B$  collisions compared to  $p + p$  and  $p + A$  collisions it is important to take into account any differences in the charm quark production in each of the different systems.

Until now, open charm measurements at RHIC have been limited to mid-rapidity. Measurements at forward rapidity are interesting for a variety of reasons. First is the need to constrain theoretical calculations over a wide kinematic range. The importance of this is demonstrated by the D0 measurement of bottom production at large rapidity ( $\sqrt{s} = 1.8$  TeV,  $p_T > 5$  GeV/c,  $2.4 < y_\mu < 3.2$ ), as deduced from the production of high  $p_T$  muons [1]. Significant theoretical improvements resulted from the effort to reduce what was, initially, a discrepancy between theory and experiment that increased with increasing rapidity [5]. Second, significant cold nuclear effects have been seen in RHIC collisions at forward rapidity. PHENIX [47], BRAHMS [48, 49], and STAR [50] have all measured light hadron production in  $d + Au$  collisions at forward rapidity and have found significant deviations from  $R_{dAu} = 1$ . It will be interesting to see whether charm production follows a similar pattern. Finally, open charm production at forward rapidity needs to be understood to fully interpret PHENIX  $J/\psi$  measurements at forward rapidity [24, 25, 51, 52, 53].

In this paper we report on the measurement of muon production at forward rapidity ( $1.5 \leq |\eta| \leq 1.8$ ), in the range  $1 < p_T < 3$  GeV/c, in  $\sqrt{s} = 200$  GeV  $p + p$  collisions by the PHENIX experiment. The upper limit of the  $p_T$  range is determined by available statistics. The vertex-independent muon yield is statistically extracted by calculating and subtracting contributions from

light mesons ( $\pi$ 's and  $K$ 's) which decay into a muon, and hadrons which penetrate through the muon arm absorber material. In the absence of new physics, and in the  $p_T$  range measured in this analysis, such muons come dominantly from the decay of hadrons containing a charm quark (with small contributions from decays of hadrons containing a bottom quark and decays of light-vector mesons). PYTHIA is used to determine the charm quark spectrum that would produce the observed vertex-independent muon spectrum, and from this we obtain the differential cross section of charm quark production at forward rapidity.

The remainder of this paper is organized as follows: In Section II we describe the PHENIX experimental apparatus, with special emphasis on the muon arm detectors. In Section III we describe the methodology used to extract the vertex-independent muon signal. This section includes details on the run, event and track selection criteria; values obtained for contributions to the muon yield from abundant light hadrons, which are subtracted to obtain the vertex-independent muon yield; and details on the systematic error analysis. In Section IV we extract the differential cross section for charm production at  $y = 1.6$ , integrated over  $p_T$ . Finally, in Section V we compare to other measurements, draw conclusions, and discuss the prospects for such measurements with improved data sets currently under analysis.

## II. THE PHENIX EXPERIMENT

The PHENIX experiment [54], shown in Figure 1, is a large multipurpose set of detectors optimized for measuring relatively rare electromagnetic probes (photons, muons, and electrons) of the spin structure of the proton and of the hot dense matter created in ultrarelativistic heavy ion collisions. The data acquisition system and multilevel triggers are designed to handle the very different challenges presented by  $p + p$  collisions (relatively small events at very high rates) and  $Au + Au$  collisions (very large events at relatively low rates) with little or no deadtime [55, 56]. Event characterization devices, such as the Beam-Beam Counters [57] used in this analysis, provide information on the vertex position, start time, and centrality of the collision. The two muon arms cover  $1.2 < |\eta| < 2.4$  in pseudorapidity and  $\delta\phi = 2\pi$  in azimuth. The two central arms, which each cover  $|\eta| < 0.35$  and  $\delta\phi = \pi/2$ , are not used in this analysis.

The Beam-Beam Counters (BBCs) [57] each consist of 64 quartz radiators instrumented with mesh dynode PMTs and arranged in a cylinder coaxial with the beam. The BBCs are placed on either side of the collision vertex and cover  $3.0 < |\eta| < 3.9$ . Each channel has a dynamic range extending to 30 MIPs. The BBCs measure the arrival times of particles on both sides of the collision vertex,  $t_S$  and  $t_N$ . From the average of these times we determine the event start time. From their difference we obtain the position of the vertex along the beam di-

rection,  $z_{vtx}$ . The BBCs also provide the minimum bias interaction trigger, which requires that there be at least one hit in each BBC and that  $|z_{vtx}| < 38$  cm.

The muon arms [58] are coaxial with the beam on opposite sides of the collision vertex. By convention the arm on the South (North) end of the interaction region is assigned negative (positive)  $z$  coordinates and rapidity. For the 2001/2 run period, in which the data for this paper were collected, only the South muon arm was operational. Each muon arm is comprised of a Muon Tracker (MuTR) and a Muon Identifier (MuID). The MuTR makes an accurate measurement of particle momenta. The MuID allows coarse resolution track reconstruction through a significant amount of steel absorber. Together the muon arm detectors provide significant pion rejection ( $> 250 : 1$ , increasing with decreasing momentum) through a momentum/penetration-depth match.

Before ever reaching the MuTR detectors a particle must pass through the pre-MuTR absorber: 20 cm of copper (the nosecone) plus 60 cm of iron (part of the MuTR magnet). The nominal nuclear interaction lengths of iron and copper are  $\lambda_I^{Fe} = 16.7$  cm and  $\lambda_I^{Cu} = 15.3$  cm (although this varies with particle species and energy, see Section III F). Therefore the pre-MuTR absorber presents a total thickness of  $4.9\lambda_I / \cos\theta$ , where  $\theta$  is the polar angle of a particle's trajectory. This absorber greatly reduces the MuTR occupancy and provides the first level of pion rejection.

Each MuTR arm consists of three stations of cathode strip chambers installed in an eight-sided conical magnet [59]. The radial magnetic field ( $\int \mathbf{B} \cdot d\mathbf{l} = 0.72$  T·m at 15 degrees,  $B(\theta) \approx B(15^\circ) \tan(\theta) / \tan(15^\circ)$ ) bends particles in the azimuthal direction. Each station occupies a plane perpendicular to the beam axis and consists of multiple ionization gaps (3 gaps for the two stations closest to the collision vertex, 2 gaps for the last station) which have their charge imaged on two cathode strip planes oriented with a small stereo angle to provide two-dimensional information. An ionizing particle typically fires three adjacent strips in each orientation. A fit to the charge distribution on adjacent strips provides a position measurement with a resolution of  $\sigma \approx 100 \mu\text{m}$  in the bend direction. The MuTR achieves a momentum resolution of  $\sigma_p/p \approx 5\%$  over the analyzed kinematic range. The resolution is approximately independent of momentum due to the significant contribution from energy loss fluctuations in the pre-MuTR absorber, which falls as  $1/p$ , and which counters the more familiar linear momentum dependence seen for particles tracked through a "thin" detector.

Each MuID arm consists of five steel absorber plates interleaved with Iarocci tubes (operated in proportional mode) and specialized shielding to reduce backgrounds not originating from the collision vertex. Gaps are labeled 0–4 proceeding downstream from the collision point.

The Iarocci tubes, which are between 2.5 and 5 m in length, have eight  $1 \text{ cm}^2$  square cells, each consisting of a

## PHENIX Detector - Second Year Physics Run

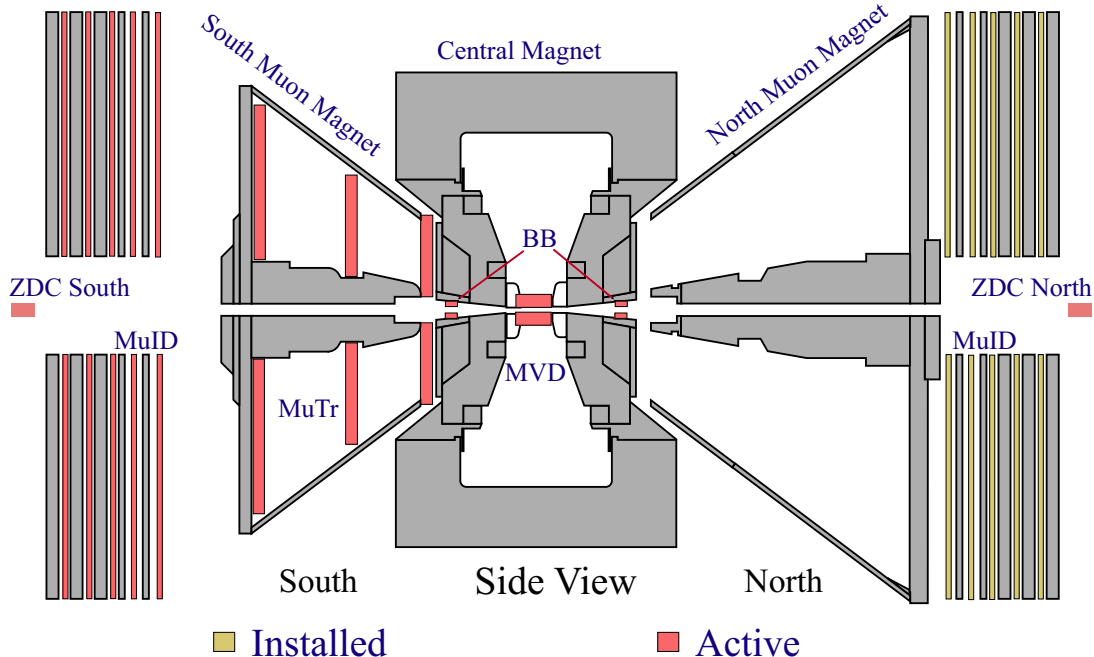


FIG. 1: (Color online) PHENIX experimental layout during the 2001/2 run period.

three-sided ground electrode and an anode wire, mounted inside a PVC gas enclosure. A readout channel (“two-pack”) is formed by wire-ORing the 16 anode wires of two tubes which are mounted in planes perpendicular to the beam axis and staggered by half of a cell width (0.5 cm). This provides redundancy, eliminates geometric inefficiency due to the cell walls, and reduces the maximum drift time for charge collection. Digital readout of the two-pack signals provides a coarse one-dimensional hit position ( $\sigma = 9 \text{ cm}/\sqrt{12} = 2.6 \text{ cm}$ ). The tubes in each gap are mounted in six individual panels, each of which contains two layers of two-packs (horizontally and vertically oriented), thus providing two-dimensional information.

The first MuID absorber plate (thickness = 20 cm - South; 30 cm - North) also serves as the return yoke of the MuTR magnet. Successive plates (identical for the two arms) are 10, 10, 20 and 20 cm thick, thus totaling  $4.8\lambda_I/\cos\theta$  ( $5.4\lambda_I/\cos\theta$ ) for the South (North) arm. Due to ionization energy loss a particle must have a momentum at the vertex which exceeds  $2.31 \cos\theta \text{ GeV}/c$  ( $2.45 \cos\theta \text{ GeV}/c$ ) to penetrate to the most downstream MuID gap of the South (North) arm.

Steel plates surrounding the beam pipe guard against backgrounds caused by low-angle beam-beam collision products which scrape the beam pipe near the MuID  $z$ -location (7-9 m) or shine off the RHIC DX magnets immediately downstream of each MuID arm. Steel blocks in the RHIC tunnels guard against penetrating radiation generated by the incoming beams scraping against beamline components (primarily the final focus-

ing quadrupoles).

The MuID also contributes information to the first-level trigger decision. For the 2001/2 run, during which the data for this analysis were collected, a relatively coarse trigger was implemented using LeCroy 2372 Memory Lookup Units (MLUs). Each gap was divided into quadrants with a horizontal and vertical split going through the beam axis. Signals from tubes in an individual gap/orientation (layer) and quadrant were logically combined. Only gaps 0,2,3 and 4 were used in the trigger due to the 16-bit input limitation of the MLUs. The penetration depth required for the trigger to fire was programmable. The *MuID-1Deep* trigger fired if more than 6 out of 8 layers in a particular quadrant were hit (indicating the possibility that the event contained a particle penetrating to MuID gap 4). The *MuID-1Shallow* trigger fired if 3 of the 4 most shallow layers (horizontal and vertical layers in gaps 0 and 2) were hit for a particular quadrant.

### III. METHOD FOR EXTRACTION OF MUONS FROM CHARM DECAY

Inclusive muon candidates,  $N_I$ , are those particles which are successfully reconstructed to the last MuID gap (gap 4). These consist of four components: 1) “free-decay muons”,  $N_D$ , which result from the decay of light hadrons ( $\pi$  and  $K$  mesons) before reaching the pre-MuTR absorber, 2) “punchthrough hadrons”,  $N_P$ , which penetrate the entire detector and are thus misidentified as muons

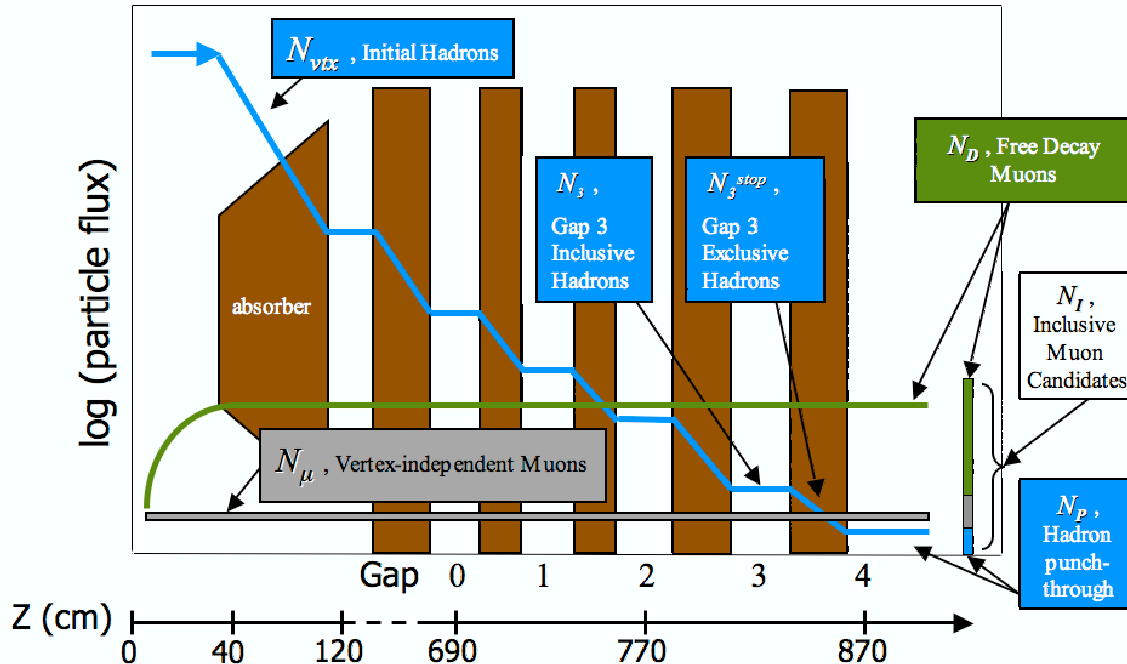


FIG. 2: (Color online) Schematic depiction of the relative flux of different components of the inclusive muon candidate yield as a function of flightpath into the muon arm absorber (the event vertex is at  $z_{vtx} = 0$ ). See text for details.

3) “background tracks”,  $N_B$ , which in  $p + p$  collisions are dominated by hadrons which decay into a muon after reaching the MuTR, and 4) “vertex-independent muons”,  $N_\mu$ , which are primarily due to the decay of heavy flavor mesons.

Figure 2 shows a schematic depiction of the relative yield per event of these different contributions as a function of flightpath into the muon arms, as described below.

The number of hadrons is large and essentially independent of flightpath until the first absorber layer is reached. In each absorber layer these hadrons undergo strong interactions with a probability  $1 - \exp(-L/\lambda)$ , where  $L$  is the length of absorber material traversed, and  $\lambda$  is the species and  $p_T$ -dependent nuclear interaction length determined in Section III F. Most of these interacting hadrons are effectively eliminated as possible muon candidates. However, a small fraction of hadrons penetrate the entire absorber thickness. These punchthrough hadrons are indistinguishable from muons.

The decay lengths for  $\pi$ 's ( $c\tau = 780\text{cm}$ ) and  $K$ 's ( $c\tau = 371\text{cm}$ ) are long compared to the flightpath from the vertex to the absorber. Therefore, the fraction of decay muons from these sources is relatively small, but increases linearly with the flightpath until the first absorber layer is reached. A hadron which decays prior to the pre-MuTR absorber into a muon that is inside the detector acceptance is indistinguishable from a muon originating at the vertex. After the first absorber layer the number of free-decay muons remains constant by definition.

Hadrons which decay in the MuTR volume are a relatively small contribution since most are absorbed prior to reaching the MuTR, the Lorentz-dilated decay lengths are long compared to the length of the MuTR volume (South  $\approx 280\text{cm}$ , North  $\approx 420\text{cm}$ ), and a particle which decays in the MuTR is less likely to be reconstructed. Such tracks are partially accounted for in the calculation of punchthrough hadrons (see Section III F) and the remaining fraction falls under the category of background tracks (Section III G). This small contribution is not shown.

Without a high-resolution vertex detector muons from various sources (the decay of open heavy flavor hadrons, the decay of quarkonia, the decay of light vector mesons, and Drell-Yan production) originate indistinguishably close to the collision vertex. Thus their yield is independent of the flightpath and independent of the vertex position. Since inclusive muon candidates, by definition, penetrate to MuID gap 4, we measure the combined yield at  $z \approx 870\text{cm}$ .

Figure 3 shows a sample distribution of the inclusive muon candidate yield as a function of collision vertex ( $z_{vtx}$ ), and its decomposition into the four different contributions. The yield of free-decay muons is seen to have a linear dependence that is set to 0 at  $z_{vtx} = z_{abs} - \lambda_D$ . Here  $z_{abs} = -40\text{cm}$  is the upstream face of the pre-MuTR absorber (indicated by the thick solid line), and  $\lambda_D$  is the effective absorption length, beyond which there are no free-decay muons.  $\lambda_D$  was found to be nearly iden-

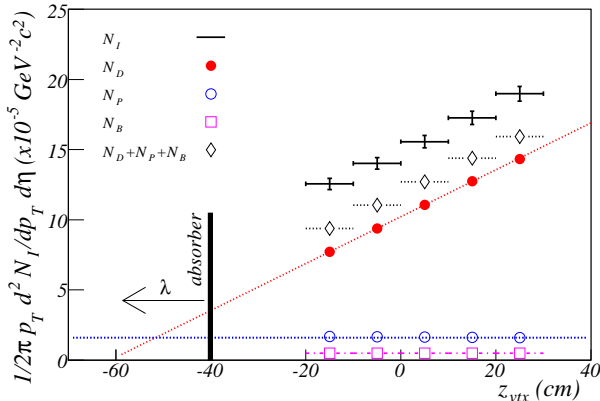


FIG. 3: Sample  $z_{vtx}$  distribution of different components of the inclusive muon candidate yield (measured data for both charge signs over the range  $1.0 < p_T < 1.2 \text{ GeV}/c$ ). Crosses show inclusive muon candidates, filled circles show free-decay muons, open circles show punchthrough hadrons, open squares show background tracks, and open diamonds show the sum of these three hadronic sources. The vertex-independent muon yield is obtained from the difference between the yield of inclusive muon candidates and the yield of light hadronic sources.

tical to the species and  $p_T$ -dependent nuclear interaction lengths determined in Section III F. Muons originating from meson decays downstream of this location have no  $z_{vtx}$  dependence. The fraction not accounted for in the calculation of the punchthrough hadron yield forms the small contribution from background tracks. The yield

$$N_\mu(p_T) = \frac{1}{N_{z_{vtx}}} \sum_{j=1}^{N_{z_{vtx}}} N_I(p_T, z_{vtx}^j) - N_D(p_T, z_{vtx}^j) - N_P(p_T, z_{vtx}^j) - N_B(p_T, z_{vtx}^j), \quad (2)$$

where  $d^2/2\pi p_T dp_T d\eta$  is implicit in all terms of the equation.

We convert this into a cross section via

$$\frac{d^2 \sigma_\mu(p_T)}{2\pi p_T dp_T dy} = \frac{\sigma_{BBC}^{pp}}{\varepsilon_{BBC}^{c, \bar{c} \rightarrow \mu}} \frac{d^2 N_\mu(p_T)}{2\pi p_T dp_T d\eta}. \quad (3)$$

Here  $\sigma_{BBC}^{pp}$  is the cross section of the BBC trigger for  $p + p$  interactions and  $\varepsilon_{BBC}^{c, \bar{c} \rightarrow \mu}$  is the efficiency of the BBC trigger for events in which a charm quark is created and decays into a muon. Substituting  $\eta \rightarrow y$  introduces negligible error due to the small mass of the muon, the only component left after the subtraction. As described in Section III I, systematic errors are determined for each component and combined into a term that applies to the overall normalization and a term that applies to the  $p_T$  dependence of the spectrum.

of punchthrough hadrons and vertex-independent muons also have no  $z_{vtx}$  dependence. Note that the ratio of different contributions to the inclusive muon candidate spectrum is  $p_T$  dependent.

In order to extract the cross section for charm production we first need to determine the yield of vertex-independent muons,  $N_\mu(p_T)$ , the amount beyond that due to light hadrons and fake backgrounds. As described in Section III A, we select good runs, events, and tracks, and restrict our acceptance to regions where the detector performance was optimal, and the acceptance vs.  $z_{vtx}$  was nearly constant. Next, as described in Sections III B and III C, we obtain the yield of inclusive muon candidates vs.  $p_T$  and  $z_{vtx}$ , corrected for acceptance and efficiency:  $N_I(p_T, z_{vtx})$ . In Section III D we describe a data-driven hadron generator. This generator is used in Section III E, in which we describe how the vertex dependence of the inclusive muon candidate yield allows us to obtain the yield of muons from light-meson decay before the pre-MuTR absorber, similarly corrected and binned:  $N_D(p_T, z_{vtx})$ . This generator is also used in Section III F, in which we describe how we use hadrons which stop in MuID gap 3 (the penultimate gap), together with simulations of hadron penetration in the MuID absorber, to obtain the yield of punchthrough hadrons in MuID gap 4:  $N_P(p_T, z_{vtx})$ . The yield of fake tracks,  $N_B(p_T, z_{vtx})$ , determined from simulations described in Section III G, is found to be small.

The yield of vertex-independent muons is determined by subtracting the contributions from light hadrons and fake backgrounds and averaging over  $z_{vtx}$  bins:

We use PYTHIA to derive the  $p_T$ -dependent differential cross section for the production of charm quarks responsible for the vertex-independent muon yield. This procedure is very similar to that in references [7, 8, 9, 10, 11, 12, 13], and is described in detail, along with the associated systematic error analysis, in Section IV.

## A. Data Reduction

### 1. Data Sets and Triggering

Runs were selected for this analysis based on stable detector operation using the same criteria as an earlier analysis of  $J/\psi$  production [51]. Further runs were eliminated due to the presence of large beam-related back-

grounds entering the *back* of the detector.

We select only those events in the vertex range  $-20 < z_{vtx} < 30$  cm. This minimizes the  $z_{vtx}$  dependence of the detector acceptance and allows us to treat the amount of absorber material as a simple function of polar angle, ignoring complications in the pre-MuTR absorber near the beampipe.

The decision to collect an event was made by the Local Level-1 Trigger [55] within  $4 \mu\text{s}$  of the collision. Input to the trigger decision was given by the BBC (collision with a valid event vertex) and the MuID (reconstructed penetrating track). Each trigger could be independently scaled down, so that it occupied a predetermined fraction of the available bandwidth, by selecting every  $N_i^{th}$  instance, where  $N_i$  is the scaledown factor for the  $i^{th}$  trigger. Three different data sets were selected from the good runs for different aspects of the data analysis:

- *BBC*: To extract  $N_D$  we need to measure the  $z_{vtx}$  dependence of  $N_I$ . For this we need the unbiased collision vertex distribution, which we obtain from a set of events collected with the *BBC* trigger:  $N_{BBCN} > 1$  &&  $N_{BBCS} > 1$  &&  $|z_{vtx}| < 38$  cm, where  $N_{BBCN}$  and  $N_{BBCS}$  are the number of hits in the North and South BBC respectively.  $\sigma_{BBC}^{pp}$  was found to be  $21.8 \pm 2.1$  mb using a van der Meer scan [60]. There were  $1.72 \times 10^7$  *BBC* triggered events passing our vertex selection criteria in this data set, corresponding to a sampled luminosity of  $\int L dt = 0.79 \text{ nb}^{-1}$ .
- *MuID-1Deep* && *BBC (M1D)*: In order to extract  $N_I$ ,  $N_D$  and  $N_B$  we used events selected with the *M1D* trigger, which enriched the sample of events with tracks penetrating to MuID gap 4. For the *M1D* and *BBC* data sets we used identical run selection criteria. The total number of sampled *BBC* triggers for this data set was  $5.77 \times 10^8$ , corresponding to a sampled luminosity of  $\int L dt = 26.5 \text{ nb}^{-1}$ .
- *MuID-1Shallow* && *BBC (M1S)*: In order to extract  $N_P$  we need a data set which provides an unbiased measurement of the number of particles which penetrate to MuID gap 3. Since the *M1D* trigger required tracks to penetrate to MuID gap 4 it could not be used. Instead we used the *M1S* trigger, which only used information from MuID gaps 0-2. We used a subset of runs for which the scaledown factor for this trigger was only 10, corresponding to a sampled luminosity of  $\int L dt = 1.72 \text{ nb}^{-1}$ .

## 2. Track Selection

The Muon arm reconstruction algorithm starts by finding “roads” (collections of hits in the MuID which form straight, two-dimensional lines) and then combining them with hits in the MuTR to form “tracks”. We

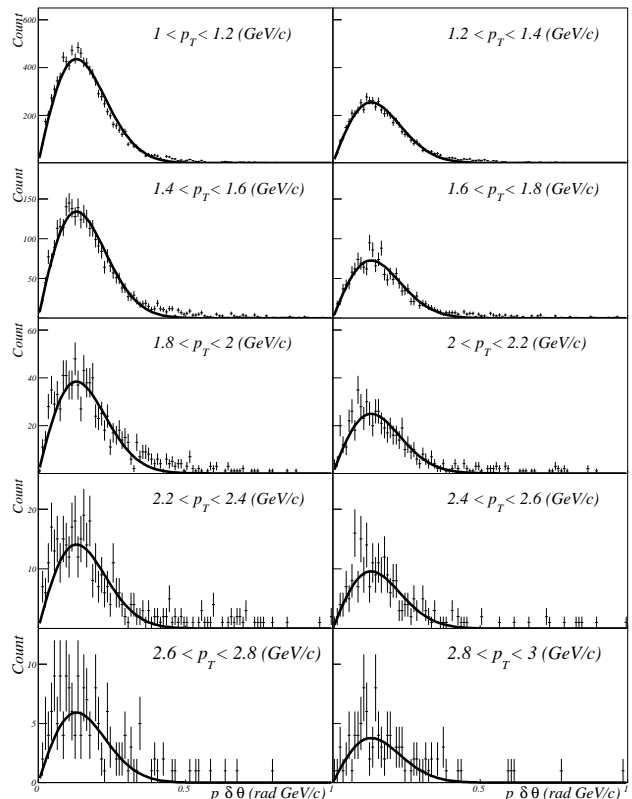


FIG. 4: The scaled angular deflection is the difference in a particle’s polar angle caused by passage through the pre-MuTR absorber scaled by the particle’s momentum,  $p\delta\theta$ . For muons (and hadrons not undergoing a strong interaction in the pre-MuTR absorber) one expects the distribution of this quantity to be well described by the standard multiple scattering formula. The different panels show  $p\delta\theta$  for different  $p_T$  bins with fits (normalization only) to the expected distribution.

apply strict cuts on both road and track parameters in order to reduce backgrounds, see Table I.

The resulting purity of the selected tracks is demonstrated in Figure 4. This figure shows  $p\delta\theta$ , the angular deviation through the pre-MuTR absorber, scaled by the particle momentum to give a quantity which should be momentum independent, for different  $p_T$  bins. As shown in Figure 5,  $\delta\theta$  is the angular difference between the reconstructed particle trajectory at the collision vertex ( $x = 0, y = 0, z = z_{vtx}$ ) and at MuTR station 1. A GEANT [61] simulation of the PHENIX detector showed that tracks which do not suffer a strong interaction in the pre-MuTR absorber undergo angular deviations consistent with expectations based on standard multiple scattering:  $\sigma_{\delta\theta} \propto \sqrt{x/X_0}/p$ . The curves in each panel are fits to  $Cp\delta\theta \exp(-(p\delta\theta)^2/2(p\sigma_{\delta\theta})^2)$ , in which the normalization constant ( $C$ ) is allowed to float, and  $p\sigma_{\delta\theta} = 130 \text{ rad}\cdot\text{MeV}/c$  is given by GEANT and is consistent with a simple estimate based on the radiation length of the pre-MuTR absorber and the standard multiple scattering formula [62, 63, 64] ( $x/X_0 \approx 48 \rightarrow p\theta_{space}^{rms} \approx$



TABLE I: Road and track cuts. Here  $D_p$  is the penetration depth, defined to be the most downstream MuID gap with at least one hit (from the horizontal or vertical layer) associated with the track;  $z$  is the coordinate along the beam;  $x$  and  $y$  are transverse to each other and to the beam axis; the vertex cut refers to the transverse position of the MuID road projected to the  $xy$  plane at  $z = 0$ ; and the slope cut refers to the direction cosine of the road in each transverse direction.

	# Associated MuID hits, $N_{MuID} > 6$ (out of a possible $2D_p$ )
Road cuts	Vertex cut, $\sqrt{x^2 + y^2} < 100$ cm @ $z = 0$ Slope cut, $\sqrt{(\frac{dx}{dz})^2 + (\frac{dy}{dz})^2} > 0.25$ $\geq 1$ associated hit in MuID gap 4
Track cuts	Track fit quality, $\chi^2/\text{dof} \leq 10$ # Associated MuTR hits, $N_{MuTR} > 12$ (out of a possible 16)

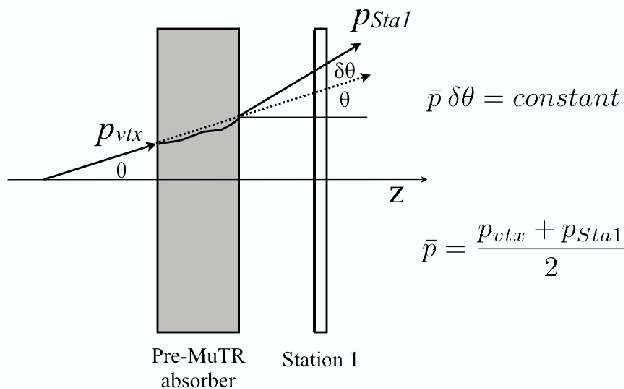


FIG. 5: The angular deflection,  $\delta\theta$  is the angular difference between the reconstructed particle trajectory at the collision vertex and at MuTR station 1. The momentum used to scale  $\delta\theta$  is the average of the momentum reconstructed inside the MuTR magnet ( $p_{sta1}$ ) and the momentum extrapolated to the vertex ( $p_{vtx}$ ).

$(\sqrt{2})(13.6 \text{ MeV}/c)(\sqrt{48}) \text{ rad} = 133 \text{ rad}\cdot\text{MeV}/c$ . The integral beyond  $3p\sigma_{\delta\theta}$  is  $\approx 5\%$  and is largely due to hadrons which have a strong interaction in the pre-MuTR absorber and are still reconstructed as a muon candidate. Such tracks are accounted for in the calculation of the punchthrough hadron yield, as described below.

### 3. Acceptance Restriction

We further restricted the acceptance of muon candidates for this analysis in two ways:

1. We required tracks to pass through  $\theta/\phi$  regions in which the Monte Carlo detector response strictly agreed with the measured response. This was established by agreement between the number of data

hits and Monte Carlo hits assigned to tracks in each  $\theta/\phi$  region of the detector.

2. We required tracks to lie within a pseudorapidity range,  $1.5 < |\eta| < 1.8$ , a region over which the acceptance depends only weakly on the collision  $z_{vtx}$  location.

## B. Acceptance and Efficiency

We factorized the acceptance and efficiency for tracks penetrating to a particular MuID gap,  $i$ , into four components:

1.  $\varepsilon_{\text{acc}}^i$ : the acceptance of a perfectly working detector with the acceptance restrictions described above. This quantity ( $\approx 50\%$ ) is normalized to  $2\pi\delta\eta$  ( $\delta\eta = 0.3$ ) and accounts for non-sensitive structural members in between the cathode strip chambers and chamber regions removed from consideration for the entirety of this analysis.
2.  $\varepsilon_{\text{rec}}^i$ : the efficiency of reconstructing a track that fell within the accepted region. This quantity is somewhat low (64%) due to detector problems in this first physics run that have been subsequently resolved.
3.  $\varepsilon_{\text{user}}^i$ : the efficiency for reconstructed tracks to pass the cuts listed in Table I.
4.  $\varepsilon_{\text{trig}}^i$ : the efficiency of the MuID trigger to fire in events with selected tracks.

$\varepsilon_{\text{acc}}^i$ ,  $\varepsilon_{\text{rec}}^i$ , and  $\varepsilon_{\text{user}}^i$  were evaluated with a GEANT simulation using single muons thrown with a realistic  $p_T$  spectrum into the muon arms. The applied detector response incorporated measured detector performance. Reductions in efficiency due to occupancy are negligible in  $p+p$  collisions. Run-to-run variations were ignored since we selected runs in which the detector performance was similar and stable. Efficiency values for tracks penetrating to MuID gap 4 were parameterized in terms of  $z_{vtx}$  and  $p_T$  and are listed in Table II. There are minor differences in these parameterizations for particles with different charge sign.

We also determined the efficiencies for tracks which only penetrate to MuID gap 3, since these are needed to obtain the yield of punchthrough hadrons. These were found to scale from the efficiencies for tracks penetrating to MuID gap 4:  $\varepsilon_{\text{acc}}^3 \varepsilon_{\text{rec}}^3 \varepsilon_{\text{user}}^3 = \varepsilon_{\text{scale}}^3 \times \varepsilon_{\text{acc}}^4 \varepsilon_{\text{rec}}^4 \varepsilon_{\text{user}}^4$ , where  $\varepsilon_{\text{scale}}^3 = 0.66$ .  $\varepsilon_{\text{scale}}^3$  is less than one because the MuID and the road reconstruction algorithm are optimized for deeply penetrating particles. Particles which do not penetrate to the last gap have poorer resolution matching to MuTR tracks (due to reduced lever arm and smaller number of hits) and are also more susceptible to MuID inefficiencies.

TABLE II: Trigger, acceptance, track reconstruction and track selection efficiencies. Systematic errors for these quantities are given in Tables V and VII.

Quantity	Value
$\varepsilon_{\text{acc}}^{4,+}$	$0.51 \times (1 - 114 \exp(-5.9p_T)) \times (1 + 0.0015z_{vtx})$
$\varepsilon_{\text{acc}}^{4,-}$	$0.50 \times (1 - 531 \exp(-7.5p_T)) \times (1 + 0.0013z_{vtx})$
$\varepsilon_{\text{rec}}^4$	0.64
$\varepsilon_{\text{user}}^{4,+}$	$0.74 \times (1 - 0.0019z_{vtx})$
$\varepsilon_{\text{user}}^{4,-}$	$0.74 \times (1 - 0.0009z_{vtx})$
$\varepsilon_{\text{scale}}^3$	0.66
$\varepsilon_{\text{trig}}^4$	0.86
$\varepsilon_{\text{trig}}^3$	0.97
$\varepsilon_{BBC}^{c,\bar{c} \rightarrow \mu}$	0.75

Trigger efficiencies,  $\varepsilon_{\text{trig}}^3$  and  $\varepsilon_{\text{trig}}^4$ , are also listed in Table II. These were evaluated using the *BBC* data set, which did not require the MuID trigger to fire.

$$\varepsilon_{\text{trig}}^4 = \frac{(N_4|_{MID}) \times S_{MID}}{(N_4|_{BBC}) \times S_{BBC}}, \quad (4)$$

where  $N_4|_{MID}$  is the number of selected tracks penetrating to MuID gap 4 for events in which the *MID* trigger fired,  $S_{MID}$  is the scaledown factor applied to the *MID* trigger, and similarly for  $MID \rightarrow BBC$ .  $\varepsilon_{\text{trig}}^3$  was also evaluated according to Equation 4, but with  $N_4 \rightarrow N_3$ , and  $MID \rightarrow MIS$ .

Since both the *MID* and *MIS* triggers required the *BBC* trigger in coincidence with the MuID trigger we must also account for the *BBC* trigger efficiency for events in which a reconstructed muon is created via charm quark decay:  $\varepsilon_{BBC}^{c,\bar{c} \rightarrow \mu}$ . The BBC efficiency was evaluated for events in which a  $J/\psi$  was produced in the muon arm acceptance using PYTHIA+GEANT simulations [51]. The BBC efficiency was also evaluated for events in which  $\pi^0$ 's were produced in the central arm acceptance [60] using data triggered without a BBC requirement. The BBC efficiency under both conditions was found to have a similar value that we therefore adopt:  $\varepsilon_{BBC}^{c,\bar{c} \rightarrow \mu} = 0.75$ .

Systematic errors for all acceptance and efficiency corrections are discussed in Section IIII and listed in Tables V and VII.

### C. Inclusive Muon Candidates

We first form two sets of collision vertex ( $z_{vtx}$ ) histograms with 10 cm bins: one histogram for all interactions selected with the *BBC* trigger, and a series of histograms for interactions selected with the *MID* trigger and having a good muon candidate within a  $p_T$  bin ( $1 < p_T < 3 \text{ GeV}/c$ ,  $200 \text{ MeV}/c$  bins). The muon candidate histograms are formed separately for each charge sign. Entries into each histogram are scaled by the appropriate trigger scaledown factor. The muon candidate

histograms are divided by the minimum bias histogram to give  $N_I(p_T, z_{vtx})$ , as shown in Figure 6. Systematic errors shown in this figure are discussed in Section IIII and listed in Table V.

### D. Hadron Generator

In order to determine the contributions to the inclusive muon yield from free-decay muons (Section III E), and punchthrough hadrons (Section III F) we make use of a data-driven hadron generator. The input for this generator is obtained from PHENIX measurements in  $\sqrt{s} = 200 \text{ GeV}$   $p + p$  collisions at  $y = 0$  [65, 66] using the following procedure:

1.  $\pi^+$  and  $\pi^-$  spectra at  $y = 0$  ( $0 < p_T < 3.5 \text{ GeV}/c$ ) are fit to a power law. We assume factorization in  $y$  and  $p_T$  and scale the spectra fit at  $y = 0$  according to:  

$$N_{y=1.65}^{\pi^\pm}(p_T) = N_{y=0}^{\pi^\pm}(p_T) \exp(-(1.65^2/2\sigma_y^2)),$$
with  $\sigma_y = 2.5$ . This factorization is observed both in PYTHIA and in BRAHMS [49] data measured at  $y = 1$  and  $y = 2.2$ .
2. We use a similar procedure to obtain the charged kaon yield at  $y = 1.65$ , but we need to first extrapolate the yield at  $y = 0$  beyond the current measurement limit ( $p_T < 2 \text{ GeV}/c$ ).

We start by forming the isospin averaged  $K/\pi$  ratio vs.  $p_T$  at  $y = 0$ . For  $p_T < 2 \text{ GeV}/c$  we use charged particles,  $(K^+ + K^-)/(\pi^+ + \pi^-)$  [65]. We use neutral particles,  $K^0/\pi^0$ , for  $2 < p_T < 6.5 \text{ GeV}/c$  [66]. We then fit this combined ratio to the form  $f(p_T) = A(1 - B \exp(-Cp_T))$ . Next, we normalize this function separately to the  $K^+/\pi^+$  and  $K^-/\pi^-$  ratios for  $p_T < 2 \text{ GeV}/c$ . Finally, we multiply by the corresponding charged pion spectrum to obtain  $N_{y=0}^{K^\pm}(p_T)$ , our parameterization of the mid-rapidity charged kaon  $p_T$  spectra extending out to  $3.5 \text{ GeV}/c$ .

As with pions, we need to extrapolate this parameterization of the yield at  $y = 0$  to obtain the yield at  $y = 1.65$ . One possibility is to assume boost invariance of the  $K/\pi$  ratio. However, PYTHIA gives a slightly narrower rapidity distribution for kaons than for pions, resulting in a kaon yield at  $y = 1.65$  that is only 85% of that predicted with the boost invariance assumption. We split the difference between these two assumptions:

$$N_{y=1.65}^{K^\pm}(p_T) = 92.5\% N_{y=0}^{K^\pm}(p_T) \exp(-(1.65^2/2\sigma_y^2)),$$

where, again,  $\sigma_y = 2.5$ .

3. The  $p$  and  $\bar{p}$  spectra are assumed to have the same shape as the pion spectra with normalization factors set to the measured values at  $y = 0$ ,  $p_T = 3 \text{ GeV}/c$  (0.4 for  $p/\pi^+$ , 0.24 for  $\bar{p}/\pi^-$ ) [65].

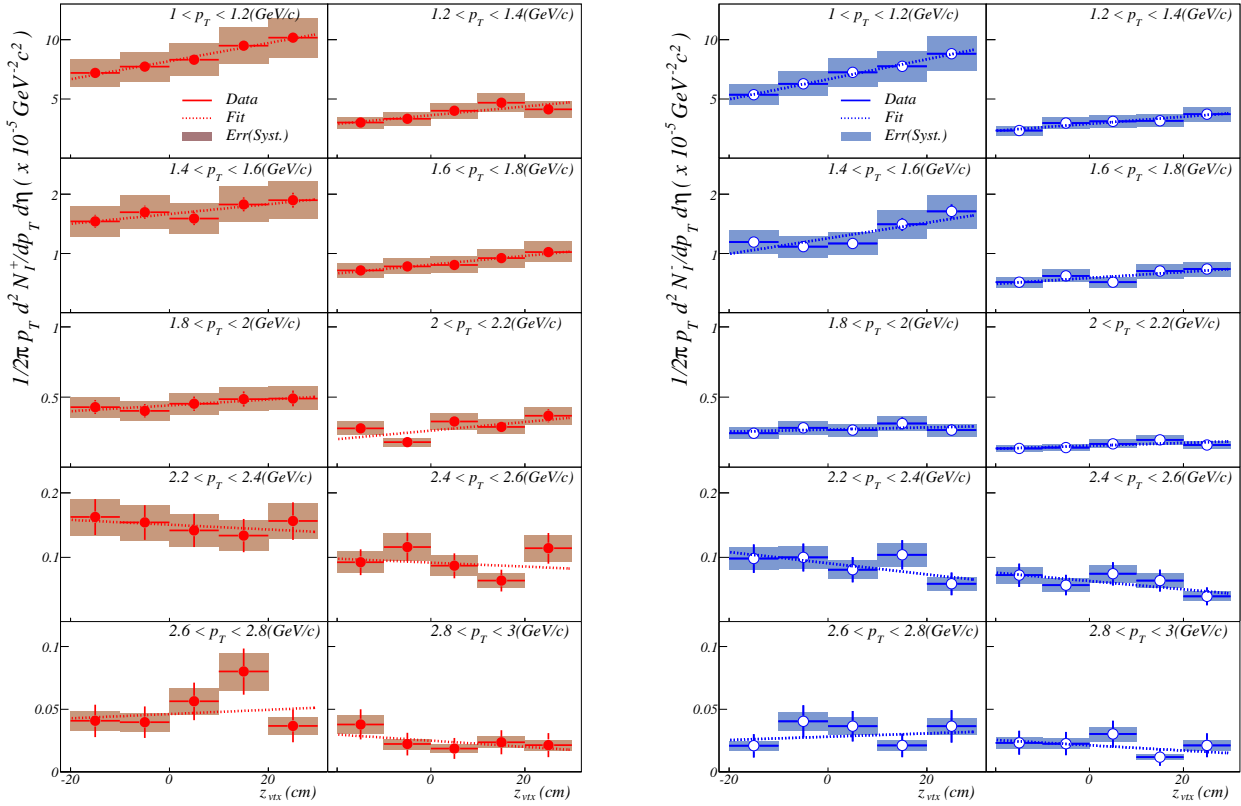


FIG. 6: Yield of (left) positively and (right) negatively charged inclusive muon candidates vs.  $z_{vtx}$  for different  $p_T$  bins. Fits shown use the functional form  $a + bz_{vtx}$  to extract the contribution from hadron decay, as discussed in Section III E. Error bars show statistical errors. Shaded bands show systematic errors, as discussed in Section III I and listed in Table V.

The exact form used for the  $p, \bar{p}$  spectra is unimportant. They obviously do not contribute to the yield of decay muons and their contribution to the yield of punchthrough hadrons is greatly suppressed due to their relatively short nuclear interaction length.

Systematic errors associated with this hadron generator are discussed in Section III I and listed in Table VI.

### E. Free-Decay Muons

In Figure 6 one can clearly see the linear dependence in the yield of inclusive muon candidates vs.  $z_{vtx}$  at low transverse momentum ( $p_T < 2$  GeV/c). This dependence is due to muons from the decay of abundant light hadrons ( $\pi$ 's and  $K$ 's) prior to the first absorber material at  $z_{abs} = -40$  cm. We fit these histograms with the function  $a + bz_{vtx}$ . After multiplying by  $dz/dl_{fp} = \cos(\langle \theta \rangle) = 0.947$  the slope,  $b$ , and its fit error give, respectively, the yield *per unit length of decay flightpath* of muons from hadron decay,  $dN_D(p_T)/dl_{fp}$ , and the statistical error on this quantity. Results are shown in Figure 7. Systematic errors shown in this figure are discussed in Section III I and listed in Table V.

This procedure does not provide a quantitative measure of the decay muon spectrum above  $p_T \sim 2$  GeV/c,

even though a substantial fraction of the inclusive muons are decay muons up to significantly higher  $p_T$ . This is due to the fact that at high  $p_T$  the decay slopes decrease (Lorentz time dilation) as do the statistics, both of which make it more difficult to quantify the decay component directly. In order to extend our estimate of decay muons to higher  $p_T$  we use our hadron generator, described in Section III D. We simulate the decay of hadrons into the muon arms and obtain predicted  $p_T$  spectra (per unit length) of muons from hadron decay separately for each charge sign. We then normalize these predicted spectra to the measured spectra. The normalized predicted spectra are shown as the dashed lines in Figure 7. The predicted spectral shape agrees with the data where we have a statistically significant measurement. The absolute normalization of the prediction is within 7% of the measured value, easily consistent within errors.

We obtain  $N_D(p_T, z_{vtx})$  from the product of  $dN_D(p_T)/dl_{fp}$  and the average value of the decay flightpath,  $l_{fp} = \lambda_D + |z_{vtx} - z_{abs}|/\cos(\theta)$ , for each  $z_{vtx}$  bin.

### F. Punchthrough Hadrons

A hadron penetrating to MuID gap 4 is impossible to distinguish from a muon. However, we can cleanly

identify hadrons in shallower gaps and then extrapolate their yield to obtain the yield of punchthrough hadrons in MuID gap 4.

Figure 8 shows the longitudinal momentum ( $p_z$ , the momentum projected onto the beam axis) distribution of particles that *stop* in MuID gap 3. The sharp peak at  $p_z \approx 2.2 \text{ GeV}/c$  corresponds to charged particles which stopped because they ranged out in the absorber plate between gaps 3 and 4 (this includes both muons and also hadrons which only suffered ionization energy loss.) The width of this peak is due to the 20 cm ( $11.4 X_0$ ) absorber thickness between MuID gaps 3 and 4, and energy-loss fluctuations in all the preceding absorber layers. Particles at momenta beyond the peak ( $p_z > 3 \text{ GeV}/c$ ) form a relatively pure sample of hadrons, with only a small contamination due to inefficiencies in MuID gap 4 and particles with mis-reconstructed momentum values. After correcting for acceptance and efficiency we use these particles to obtain the  $p_T$  spectrum for the “gap 3 exclusive yield,” as shown in Figure 9. Note: we use data from the *MIS* trigger sample since the *MID* sample required a hit in MuID gap 4, which would bias this measurement.

In order to extrapolate this measured spectrum for

hadrons stopping in MuID gap 3 to the spectrum of punchthrough hadrons which penetrate to MuID gap 4 we start by assuming exponential absorption of hadrons entering the muon arm absorber material. With this assumption we obtain an expression for the “gap 3 inclusive yield”, those hadrons that reach *at least* MuID gap 3:

$$N_3^i(p_T, \theta) = N_{vtx}^i(p_T, \theta) \exp(-L_3(\theta)/\lambda^i(p_T)), \quad (5)$$

where  $i$  indicates the contributing hadron species ( $\pi^\pm, K^\pm, p, \bar{p}$ ),  $N_{vtx}^i(p_T, \theta)$  is the yield at the vertex of the  $i^{\text{th}}$  species,  $L_3(\theta)$  is the amount of absorber material traversed to reach MuID gap 3, and  $\lambda^i(p_T, \theta)$  is the  $p_T$ -dependent nuclear interaction length of the  $i^{\text{th}}$  species. We can write a similar expression for the punchthrough hadron yield:

$$N_P^i(p_T, \theta) = N_{vtx}^i(p_T, \theta) \exp(-L_4(\theta)/\lambda^i(p_T)), \quad (6)$$

where  $L_4(\theta)$  is the amount of absorber material traversed to reach MuID gap 4.

By taking the difference between these two equations we obtain an expression for the gap 3 exclusive yield:

$$\begin{aligned} N_3^{i,stop}(p_T, \theta) &= N_3^i(p_T, \theta) - N_P^i(p_T, \theta) \\ &= N_{vtx}^i(p_T, \theta) \exp(-L_3(\theta)/\lambda^i(p_T)) \\ &\times (1 - \exp((L_3(\theta) - L_4(\theta))/\lambda^i(p_T))) \end{aligned} \quad (7)$$

In our measurement we cannot identify the species comprising the gap 3 exclusive yield, but we do know their charge sign. As a result, Equation 7 can be rewritten as two equations with six unknowns for each  $p_T$  bin:

$$\begin{aligned} N_3^{+,stop}(p_T, \theta) &= N_3^+(p_T, \theta) - N_P^+(p_T, \theta) \\ &= \sum_{i=\pi^+, K^+, p} N_{vtx}^i(p_T, \theta) \exp(-L_3(\theta)/\lambda^i(p_T)) \\ &\times (1 - \exp((L_3(\theta) - L_4(\theta))/\lambda^i(p_T))), \end{aligned} \quad (8)$$

$$\begin{aligned} N_3^{-,stop}(p_T, \theta) &= N_3^-(p_T, \theta) - N_P^-(p_T, \theta) \\ &= \sum_{i=\pi^-, K^-, \bar{p}} N_{vtx}^i(p_T, \theta) \exp(-L_3(\theta)/\lambda^i(p_T)) \\ &\times (1 - \exp((L_3(\theta) - L_4(\theta))/\lambda^i(p_T))). \end{aligned} \quad (9)$$

Based on measured cross sections for various species [67], we chose to reduce the number of unknowns with the following assumption:

$$\begin{aligned} \lambda_{K^+} &= \lambda_{long}, \\ \lambda_p = \lambda_{\pi^+} = \lambda_{\pi^-} = \lambda_{K^-} &= \lambda_{short}, \\ \lambda_{\bar{p}} &= 0. \end{aligned}$$

We further assume that  $\lambda_{short}$  and  $\lambda_{long}$  have the form  $a + b(p_T[\text{GeV}/c] - 1)$ .

We effectively smoothed the gap 3 exclusive yield for each sign by fitting the measured values to a power law. Using  $N_{vtx}^i(p_T, \theta)$  from the hadron generator (normalized to the free-decay muon spectrum, as described in Section III E) and known values for  $L_{3,4}(\theta)$ , we fit Equations 8 and 9 to the smoothed gap 3 exclusive yield for each sign to obtain:

$$\begin{aligned} \lambda_{short} &= 19.0 + 2.2(p_T[\text{GeV}/c] - 1) \text{ cm}, \text{ and} \\ \lambda_{long} &= 25.9 + 4.4(p_T[\text{GeV}/c] - 1) \text{ cm}. \end{aligned}$$

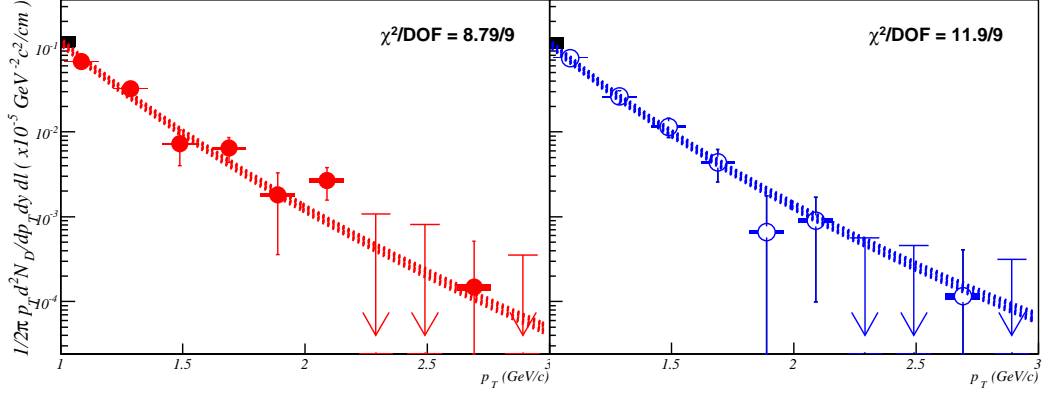


FIG. 7: Yield per unit length of (left) positively and (right) negatively charged free-decay muons. Points are the measured values determined by linear fits to the inclusive muon candidate yield (Figure 6). Error bars indicate statistical errors for those fits.  $p_T$  bins with a negative (non-physical) slope in those fits are shown with a line at the 90% C.L.U.L (statistical errors only) and an arrow pointing down. See Section III E for details. Dashed lines are the predictions for each sign from a data-driven hadron generator normalized to the measured points. The  $\chi^2/dof$  for these fits are quoted. See Section III D for details. The width of the lines corresponds to  $\sigma_{R_D}$  (see Table VI), the error on the ratio of free-decay muons to inclusive muon candidates. Black bands at the left edge of each panel show the  $p_T$ -independent systematic error on the inclusive muon candidate yield. Shaded bands on each point show the systematic errors that affect the  $p_T$  shape of the inclusive muon candidate spectrum. These last two systematic errors (Table V) need to be included in the total error budget for the yield of free-decay muons,  $\sigma_{N_D}/N_D$  (Table VI), but are displayed separately since they are common to all components of the inclusive muon candidate yield, see Equations 12 and 13. Systematic errors are discussed in Section III.

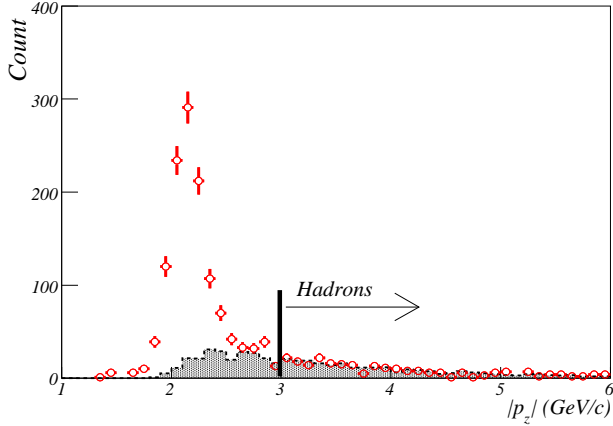


FIG. 8: Points (measured data) show the longitudinal momentum, measured at the vertex ( $p_z^{vtx}$ ), of particles that stop in MuID gap 3. The sharp peak is due to muons which range out in the absorber plate between gaps 3 and 4. The histogram (Monte Carlo) shows the longitudinal momentum of all particles that stop in MuID gap 3 and do not decay before the pre-MuTR absorber. The Monte Carlo is normalized to the data for  $p_z^{vtx} > 3$  GeV/c. Particles beyond the peak form a relatively pure sample of hadrons.

Results of these fits are shown in Figure 9.

With these values for  $\lambda_i(p_T)$  and the hadron generator input spectra, we could directly apply Equation 6 to obtain the final punchthrough spectra. However, we

made one further correction, described below, after finding that our assumption of exponential absorption does not hold when applied to GEANT simulations of the punchthrough process.

Using our GEANT-based PHENIX simulation program, we generated data sets with both the FLUKA [68] and GHEISHA [69] hadronic interaction packages. Input spectra for these data sets were given by our decay hadron generator. We selected all particles which did not decay before the pre-MuTR absorber. “Truth” values for the punchthrough and gap 3 exclusive yields were obtained by splitting those particles based on the absence (gap 3 exclusive) or presence (punchthrough) of associated charged particles with  $E_4 > 100$  MeV in MuID gap 4. We varied  $E_4$  from 50–300 MeV and saw no significant change in the results.

Using the known input spectra, known values for  $L_{3,4}(\theta)$ , and truth values for gap 3 exclusive yield, we applied Equation 7 to the Monte Carlo data sets to obtain  $\lambda_i(p_T)$ . Due to statistical limitations we integrated our results over  $\theta$  and into two  $p_T$  bins:  $1 < p_T < 2$  GeV/c and  $p_T > 2$  GeV/c. Values extracted for  $\lambda^i(p_T)$  for the different hadronic interaction packages are listed in Table III. These values are consistent with those found for our measured data, listed above.

Inserting these values for  $\lambda^i(p_T)$  into Equation 6 we obtained a prediction for  $N_P^i(p_T, \theta)$ . Ratios of the truth values and predicted values for the punchthrough yield ( $R_{N_P^i(p_T)}$ ) for the different hadronic interaction packages are listed in Table IV. One can see that these ratios deviate significantly from unity and that the two hadronic in-

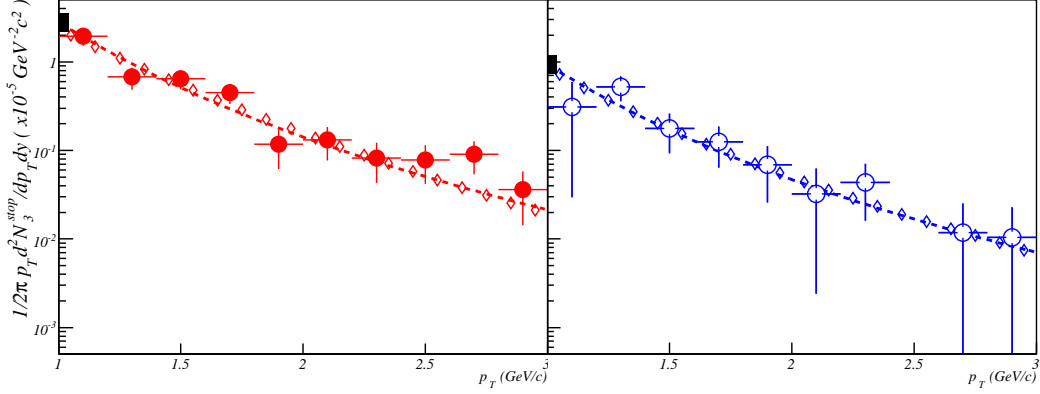


FIG. 9: Points show the  $p_T$  spectrum of (left) positively and (right) negatively charged hadrons stopping in MuID gap 3 (“gap 3 exclusive yield”) with statistical errors. Open diamonds show a power-law fit to the data, effectively a smoothed version of the data. Dashed lines are fits to the smoothed data using the hadron generator (normalized by the measured free-decay spectrum, as shown in Figure 7) and Equations 8 and 9 to obtain values for the species-dependent nuclear interaction lengths,  $\lambda^i(p_T)$ .

TABLE III: Nuclear interaction lengths,  $\lambda^i(p_T)$ , for different particle species and  $p_T$  bins (in GeV/c) for FLUKA and GHEISHA. Statistical errors on these values are  $\approx 2$  mm.

Species	FLUKA		GHEISHA	
	$\lambda^i(p_T)$ [cm]		$\lambda^i(p_T)$ [cm]	
	$1 < p_T < 2$	$p_T > 2$	$1 < p_T < 2$	$p_T > 2$
$\pi^+$	19.6	24.5	16.0	21.1
$\pi^-$	19.4	24.8	15.0	19.3
$K^+$	24.4	29.6	24.9	30.8
$K^-$	20.5	24.2	17.2	21.2

teraction packages disagree on the direction of the deviation: the exponential absorption model tends to overpredict the punchthrough yield for FLUKA ( $R_{N_P^i(p_T)}^{FLUKA} < 1$ ) and underpredict it for GHEISHA ( $R_{N_P^i(p_T)}^{GHEISHA} > 1$ ).

Relatively little data exists in the relevant momentum

range that would allow us to conclude which, if either, of the hadronic interaction package is correct. Measurements by RD10 and RD45 [70] of the penetration depth of identified hadrons found that GHEISHA did well for protons and FLUKA did not. But neither did well for pions and no data exists for kaons. Furthermore, the results are sensitive to the definition of a penetrating particle: For RD10/45 an incoming particle with any associated charged particles in the  $120 \times 120 \text{ cm}^2$  detector area at a particular depth was defined to have penetrated to that depth. In our measurement we reconstruct particle trajectories and MuID hits are not associated with a road unless they are within a narrow search window surrounding the projected trajectory. Thus we are relatively insensitive to the leakage of a showering hadron.

As a result of these uncertainties on the applicability of our exponential absorption model we incorporate a species and  $p_T$ -dependent correction factor to Equation 6:

$$N_P^i(p_T, \theta) = C^i(p_T) N_{vtx}^i(p_T, \theta) \exp(-L_4(\theta)/\lambda^i(p_T)). \quad (10)$$

The correction factors for pions and kaons are obtained from the average of the values of  $R_{N_P^i(p_T)}$  for the two packages,  $\langle R \rangle^i(p_T) = (R_{N_P^i(p_T)}^{FLUKA} + R_{N_P^i(p_T)}^{GHEISHA})/2$ , which are listed in Table IV. The values of  $\langle R \rangle^i(p_T)$  for a given species are not the same for the different  $p_T$  bins, so we assume the values are valid at the average  $p_T$  of each bin ( $p_T = 1.25 \text{ GeV/c}$  and  $2.31 \text{ GeV/c}$  respectively) and use a linear extrapolation in  $p_T$  to obtain the final correction factors:

$$C^i(p_T) = \langle R \rangle^i(1 < p_T < 2 \text{ GeV/c}) + (\langle R \rangle^i(p_T > 2 \text{ GeV/c}) - \langle R \rangle^i(1 < p_T < 2 \text{ GeV/c})) \frac{p_T[\text{GeV/c}] - 1.25}{2.31 - 1.25} \quad (11)$$

We assume that  $p$ 's and  $\bar{p}$ 's have the same correction factors as the corresponding sign pions. Since  $p$ 's and

TABLE IV: Ratios,  $R_{N_p^i(p_T)}$ , of truth values for the punchthrough hadron yield to those predicted assuming exponential hadron absorption for different particle species and  $p_T$  bins (in GeV/c), for FLUKA and GHEISHA. Average values of the ratios for the two different hadronic interaction packages,  $\langle R \rangle^i(p_T)$ , are smoothed across the  $p_T$  bin at 2 GeV/c to obtain correction factors for the exponential absorption model. Statistical errors on these quantities are  $\approx 10\%$ . The maximum fractional difference in the ratios for the two different packages (32%) is incorporated into the systematic error estimate, as shown in Table VII.

Species	$1 < p_T < 2$	$p_T > 2$	Description
$\pi^+$	0.76	0.86	$R_{N_p^i(p_T)}^{FLUKA}$
$\pi^-$	0.91	0.75	
$K^+$	0.91	1.00	
$K^-$	1.17	1.06	
$\pi^+$	1.48	1.04	$R_{N_p^i(p_T)}^{GHEISHA}$
$\pi^-$	1.47	1.09	
$K^+$	1.31	1.07	
$K^-$	2.21	1.69	
$\pi^+$	1.12	0.95	$\langle R \rangle^i(p_T)$
$\pi^-$	1.19	0.92	
$K^+$	1.11	1.04	
$K^-$	1.67	1.38	
$\pi^+$	32%	10%	$\delta R_{N_p^i(p_T)}/C^i(p_T)$
$\pi^-$	24%	18%	
$K^+$	18%	3%	
$K^-$	32%	22%	

$\bar{p}$ 's make only small contributions to the punchthrough hadrons this simplifying assumption has little consequence. We incorporate the maximum fractional difference in the ratios for the two packages (32%) into our systematic error estimate, as listed in Table VII.

We use Equation 10, with the tabulated correction factors, particle yields at the vertex given by our normalized hadron generator, the known value of  $L_4(\theta)$ , and the values for  $\lambda^i(p_T)$  determined from the measured gap 3 exclusive yield, to obtain the  $p_T$  spectrum of punchthrough hadrons,  $N_P(p_T)$ , as shown in Figure 10. Systematic errors shown in this figure are discussed in Section III and listed in Table VII. We multiply  $N_P(p_T)$  by the fraction of the accepted  $z_{vtx}$  range represented by each  $z_{vtx}$  bin to finally obtain  $N_P(p_T, z_{vtx})$ .

### G. Background Tracks

The main source of tracks which are not accounted for in the yield of punchthrough hadrons and free-decay muons, and which are not due to vertex-independent muons, are light hadrons which penetrate through the pre-MuTR absorber, decay into a muon, and are still reconstructed as a valid track.

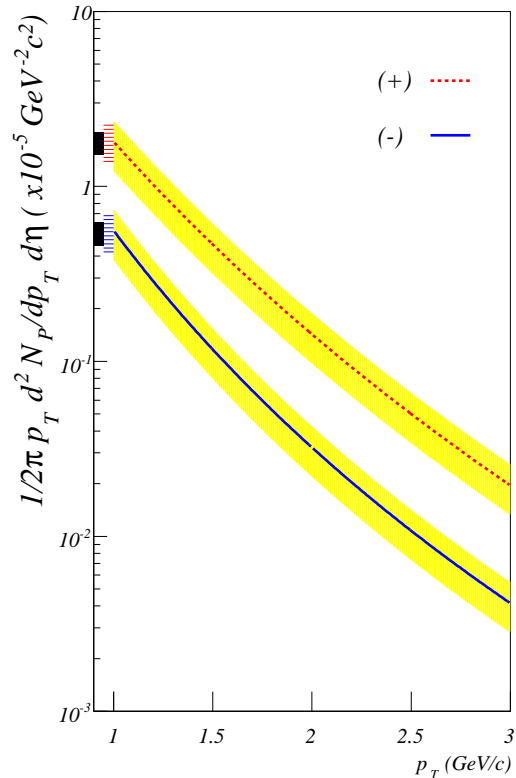


FIG. 10: Yield of positively (dotted line) and negatively (solid line) charged hadrons which penetrate to MuID gap 4. The curves are obtained from Equation 10, as described above. Solid bands on the  $y$ -axis show the relative normalization error on the inclusive muon candidate yield,  $\sigma_{N_I}^{\text{norm}}/N_I$ , see Table V. This needs to be included in the total error budget for the yield of punchthrough hadrons,  $\sigma_{N_P}/N_P$  (Table VII), but is displayed separately since it is common to all components of the inclusive muon candidate yield, see Equations 12 and 13. Hatched bands on the  $y$ -axis show  $\sigma_{R_P}^{\text{norm}}$  (see Table VII), the normalization error on the ratio of punchthrough hadrons to inclusive muon candidates. The relative fraction of positive and negative punchthrough hadrons can move up and down together by this amount. Shaded bands around the extracted punchthrough hadron yield show the systematic errors on  $\sigma_{R_P}^{p_T}$  which can affect the  $p_T$  shape of the relative fraction of positive and negative punchthrough hadrons (positives and negatives can move independently). These are dominated by differences in the applicability of the simple exponential absorption model observed for FLUKA and GHEISHA. Systematic errors are listed in Tables V and VII and discussed in Section III.

A simulation of single pions thrown into the muon arm acceptance shows that the number of hadrons which decay after the pre-MuTR absorber and penetrate to MuID gap 4 is only 5-10% (increasing with increasing  $p_T$ ) of the  $z_{vtx}$ -averaged number of free-decay muons,  $N_D(p_T, z_{vtx} = 0)$ . This ratio will be suppressed by the

fact that tracks which decay are less likely to be reconstructed successfully. It is further suppressed by our punchthrough calculation procedure: the number of such tracks which stop in MuID gap 3 is roughly half the number that penetrate to gap 4; these will be counted in our calculation of the punchthrough hadron yield.

We express our estimate for the yield of background tracks not otherwise accounted for as  $N_B(p_T) = 5\% \times N_D(p_T, z_{vtx} = 0)$ . The systematic uncertainty assigned to this quantity,  $\pm 5\% \times N_D(p_T, z_{vtx} = 0)$ , covers the extreme possibilities that the  $N_B/N_D$  is unsuppressed or fully suppressed by reconstruction and punchthrough procedures, as described above.

This estimate was verified in a simulation of  $\pi^-$ 's and  $K^-$ 's which were thrown into the muon arm acceptance and fully reconstructed. The reconstructed track information, together with the Monte Carlo truth information, allows us to eliminate uncertainties due to misreconstruction of the track  $p_T$  and due to determination of whether a track which penetrated to the last gap did so in a reconstructible fashion. Systematic errors on this estimate are discussed in Section III I.

## H. Vertex-Independent Muons

Figure 11 shows the yield of inclusive muon candidates,  $N_I(p_T, z_{vtx})$ , with contributions from individual components (free-decay muons, punchthrough hadrons, and background tracks) shown as well as their sum. The vertex-independent muons can be seen as the clear excess above the calculated background sources. The systematic error bands shown on the component sums are discussed in Section III I and listed in Tables VI and VII.

We obtain the yield of vertex-independent muons by applying Equation 2 in each  $p_T$  bin, subtracting the hadronic contributions from the inclusive muon candidate yield, and averaging over  $z_{vtx}$  bins. This yield is shown, before averaging over  $z_{vtx}$  to demonstrate the expected vertex independence, in Figure 12.

We make one final correction for momentum scale. The observed mass of the  $J/\psi$ , reconstructed with the same code and in the same data set, is higher than the nominal value by  $\approx 100$  MeV (3%) [51]. However, in a higher statistics data set the momentum scale accuracy is verified to within 1% by our observation of the accepted value for the mass of the  $J/\psi$  [52]. Also, the peak observed in the longitudinal momentum distribution of particles stopping in MuID gap 3 (see Fig. 8) is within 0.5% of the predicted value. We therefore assume that the momentum scale is high by 1.5% (splitting the difference between 0 and 3%). This results in a momentum scale correction factor to the prompt muon yield of  $0.94 + 0.987 \times (p_T[\text{GeV}/c] - 1)$ . We assume a 100% systematic error on this correction factor, as shown in Tab. V.

Finite momentum resolution can cause a similar effect. Contributions from energy loss fluctuations, multiple scattering and chamber resolution combine to give

$\delta p/p \approx 5\%$  for the momentum range used in this analysis. Finite resolution, combined with an exponentially falling spectrum, artificially hardens the measured spectrum. For  $1 < p_T < 3$  GeV/c this hardening increases the normalization of the yield by  $\approx 3.7\%$ . However, this is accounted for in our efficiency determination since we use a realistic  $p_T$  spectrum as input. Therefore we apply no explicit correction for this effect.

The final values for the vertex-independent muon cross section, obtained from Equation 3, are shown in Figure 13. Points in this figure have been placed at the average  $p_T$  value of the bin contents to account for bin shifting in the steeply falling distributions. Systematic errors shown in this figure are discussed in Section III I and listed in Tables V - VII.

## I. Systematic Errors

Many sources of systematic error on the yield of vertex-independent muons,  $N_\mu$ , are common to the different components of the inclusive muon candidate yield. In order to account for this we rewrite Equation 2 (making the  $p_T$  and  $z_{vtx}$  dependencies implicit) as:

$$\begin{aligned} N_\mu &= N_I \times (N_\mu/N_I) \\ &= N_I \times ((N_I - N_D - N_P - N_B)/N_I) \\ &= N_I \times (1 - R_D - R_P - R_B), \end{aligned} \quad (12)$$

where  $R_j = N_j/N_I$  is the fraction of the inclusive muon candidate yield attributed to the  $j^{\text{th}}$  component. We can now write the systematic error on  $N_\mu$  as:

$$\sigma_{N_\mu} = \sqrt{(\sigma_{N_I}/N_I)^2 N_\mu^2 + (\sigma_{R_D}^2 + \sigma_{R_P}^2 + \sigma_{R_B}^2) N_I^2} \quad (13)$$

$\sigma_{N_\mu}$ , as determined below, is displayed in Figures 11 and 12. Note that the errors for positives are significantly larger than for negatives. This is due to the much larger relative contribution to positive inclusive muon candidates from punchthrough hadrons, which is due to the relatively small size of the  $K^+$  nuclear interaction cross section.

Error sources contributing to  $\sigma_{N_I}$  are quantified in Table V. Error sources contributing to  $\sigma_{N_D}$  and  $\sigma_{R_D}$  are quantified in Table VI. Error sources contributing to  $\sigma_{N_P}$  and  $\sigma_{R_P}$  are quantified in Table VII. Note that in these tables we separately list errors that affect the overall normalization ( $\sigma/N^{\text{norm}}$ ) and the shape of the  $p_T$  spectrum ( $\sigma/N^{p_T}$ ). The error on  $R_B$  is taken to be 100% of its estimated value:  $\sigma_{R_B} = N_B/N_I = 0.05 \times N_D(z_{vtx} = 0)/N_I$ .

Values for  $\sigma_{N_I}/N_I$  are displayed in Figure 6. Values for  $\sigma_{R_D}$  and  $\sigma_{R_P}$  are displayed in Figures 10 and 7 respectively. We insert  $\sigma_{N_I}/N_I$ ,  $\sigma_{R_D}$ ,  $\sigma_{R_P}$ , and  $\sigma_{R_B}$  into Equation 13 as part of the final systematic error on  $N_\mu$ .

To get the vertex-independent muon cross section, as defined in Equation 3 and displayed in Figures 13 and 16, we need to add in quadrature the errors on  $N_\mu$ ,  $\sigma_{BBC}^{pp}$ ,  $\varepsilon_{BBC}^{c,\bar{c} \rightarrow \mu}$ . The error on  $N_\mu$  is obtained from the components above according to Equation 13. As mentioned



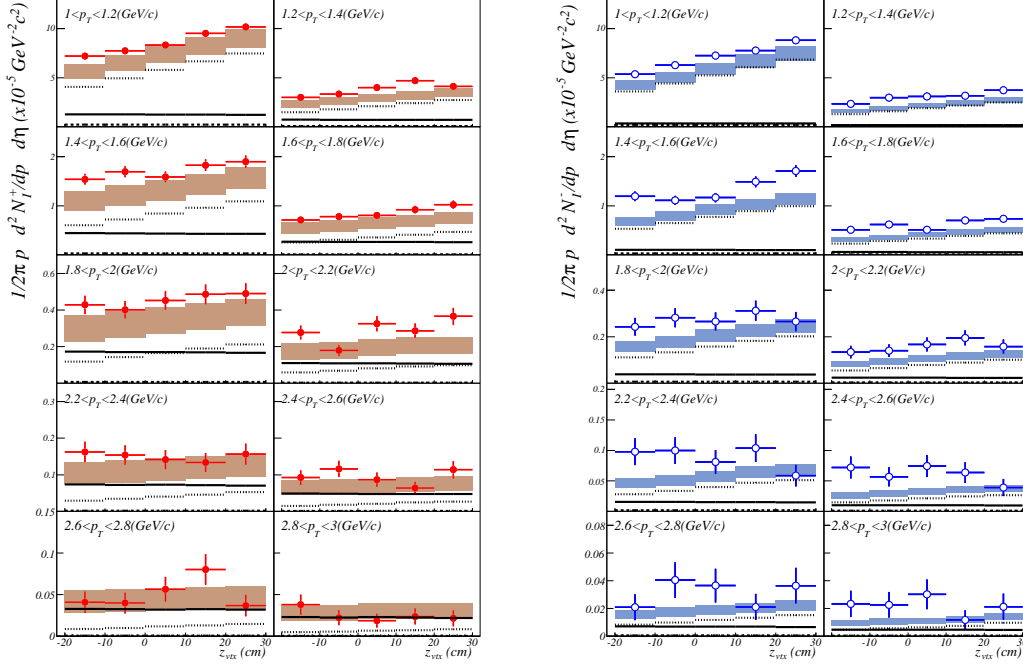


FIG. 11: Points show the yield of (left) positively and (right) negatively charged inclusive muon candidates vs.  $z_{vtx}$  for different  $p_T$  bins with statistical errors. Dotted, solid and dashed lines show contributions from decay muons, punchthrough hadrons and background tracks, respectively. Shaded bands show the systematic error around the sum of these components, as listed in Tables V-VII and discussed in Section III.

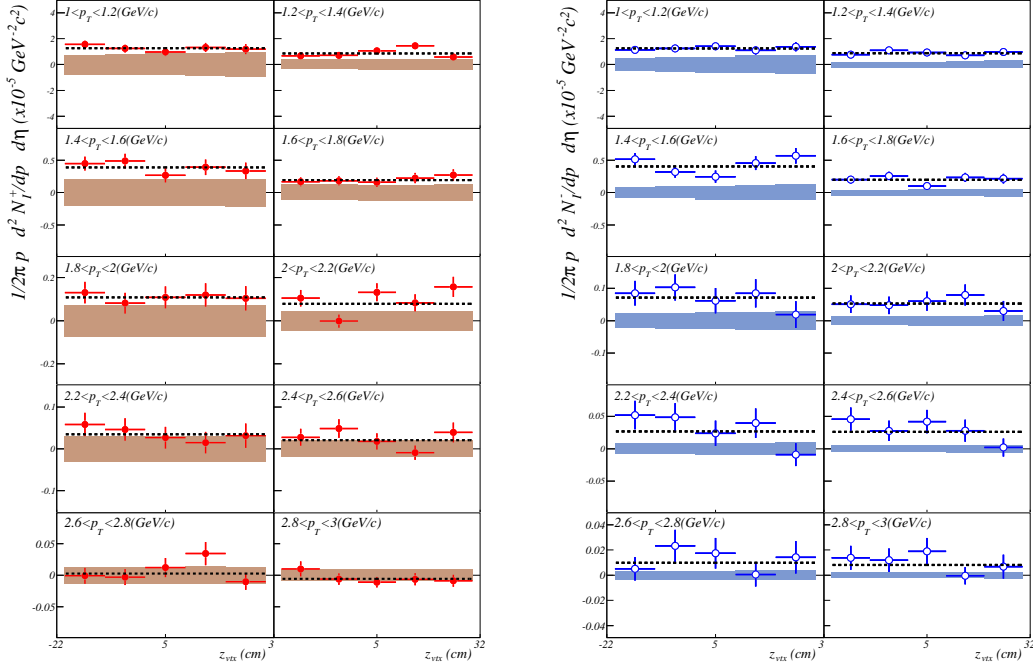


FIG. 12: Points show the yield of (left) positively and (right) negatively charged vertex-independent muons vs.  $z_{vtx}$  for different  $p_T$  bins with statistical errors. The dashed lines show the yield for each  $p_T$  bin, averaged over  $z_{vtx}$ . The shaded bands around 0 show the systematic error on the sum of the contributions to the inclusive muon candidate yield from light-hadronic sources, as listed in Tables V-VII and discussed in Section III.

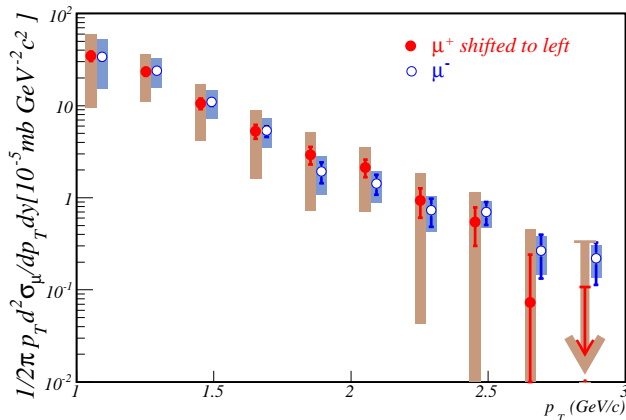


FIG. 13:  $p_T$  spectrum of vertex-independent muons. Error bars indicate statistical errors. One point with unphysical (less than zero) extracted yield is shown as an arrow pointing down from the 90% C.L.U.L. Shaded bands indicate systematic errors, as listed in Tables V-VII and discussed in Section III.

above,  $\sigma_{BBC}^{pp}$  was determined by a van der Meer scan to be 21.8 mb, with an error of 9.6% [60]. We assign an error of 5% to  $\varepsilon_{BBC}^{c,\bar{c}\rightarrow\mu}$ , which was found to be 0.75 through two different methods [51, 60].

#### IV. CHARM CROSS SECTION

The charm production cross section obtained from the yield of vertex-independent muons (or from the yield of non-photonic electrons, or  $D$  mesons) is necessarily model dependent since we do not measure the charm quarks directly. We use PYTHIA to convert our measurement of the vertex-independent muon yield into an estimate of the differential charm production cross section at forward rapidity,  $d\sigma_{c\bar{c}}/dy|_{y=1.6}$ , in a procedure very similar to that used in PHENIX measurements of charm production at  $y = 0$  [7, 8, 9, 10, 11, 12, 13]. We use PYTHIA version 6.205 with parameters tuned to reproduce charm production data at SPS and FNAL [71] and single electron data at the ISR [72, 73, 74]. Tuned parameters are listed in Table VIII. The meaning of each parameter is more thoroughly defined in the PYTHIA manual [75].

Vertex-independent muon sources, predicted by a PYTHIA simulation using the same parameters (except that MSEL is set to 2 to generate unbiased collisions), are listed in Table IX. These sources include decays of hadrons containing a heavy quark, and light vector mesons with a decay length too short to be measured with the existing experimental apparatus ( $\rho, \omega, \phi$ ). Their  $p_T$  spectra are shown in Figure 14. Contributions from quarkonium decays, Drell-Yan and  $\tau$  lepton decays are negligible. This shows that vertex-independent muon production in our acceptance is dominated by

muons from decay of charm hadrons, although for  $p_T > 2.5$  GeV/c the contribution from decays of hadrons containing a bottom quark is starting to become important.

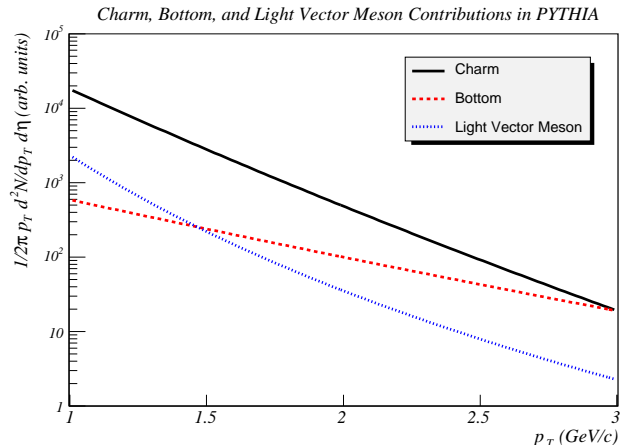


FIG. 14: PYTHIA calculation showing the major contributions to the vertex-independent muon  $p_T$  spectrum. Solid, dashed and dotted lines show the yield from charm, bottom and short-decay length light vector mesons ( $\rho, \omega, \phi$ ) respectively.

This simulation also gives the distribution of charm quarks ( $p_T$  vs.  $y$ ) that produce a muon in our acceptance, as shown in Figure 15. This demonstrates that the vertex-independent muons we measure sample charm quarks down to  $p_T \approx 1$  GeV/c, over a narrow rapidity slice centered at  $y = 1.6$ .

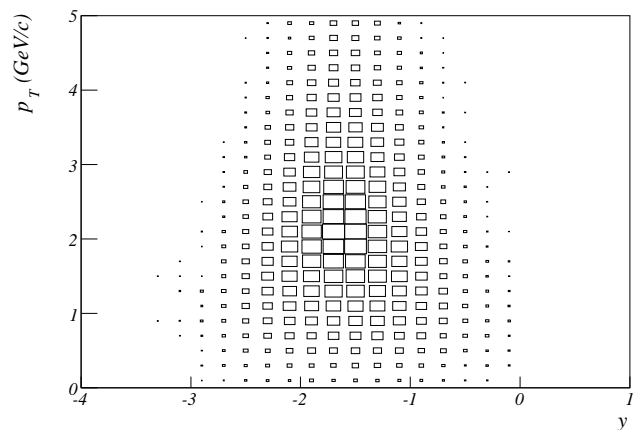


FIG. 15: PYTHIA results for the  $p_T$  vs.  $y$  distribution (linear  $z$ -scale) of charm quarks that produce a muon in the PHENIX acceptance.

Figure 16 shows a comparison of the measured vertex-independent negative muon spectrum (from Figure 13) to the prediction of this default PYTHIA simulation and to a FONLL calculation [20, 77]. One can see that the measured values significantly exceed both predictions.

TABLE V: Sources of systematic error on the calculation of  $N_I$ , the yield of inclusive muon candidates.

Error Source	$\sigma/N^{\text{norm}}$	$\sigma/N^{pT}$	Comment
Momentum Scale	6.0%	$(p_T[\text{GeV}/c] - 1) \times 1.3\%$	Taken to be 100% of the correction.
$\varepsilon_{\text{acc}}$	10%	$(p_T[\text{GeV}/c] - 1) \times 1.5\%$	Taken to be 20% of the correction.
$\varepsilon_{\text{rec}}$	9.0%	0	Taken to be 25% of the correction.
$\varepsilon_{\text{user}}$	5.0%	$(p_T[\text{GeV}/c] - 1) \times 5.0\%$	Error on $\sigma^{\text{norm}}$ taken to be 20% of the correction. Error on $\sigma^{pT}$ taken to be maximum of observed $p_T$ variation.
$\varepsilon_{\text{trig}}$	4.7%	0	Taken to be the difference in $\varepsilon_{\text{trig}}$ obtained with different procedures.
$\sigma_{N_I}/N_I$	16.3%	$(p_T[\text{GeV}/c] - 1) \times 5.4\%$	Add all rows in quadrature.

TABLE VI: Sources of systematic error on  $R_D$ , the ratio of free-decay muons to inclusive muon candidates, and  $N_D$ , the absolute yield of free-decay muons.

Error Source	$\sigma/N^{\text{norm}}$	$\sigma/N^{pT}$	Comment
Decay flight path	5%	0	Variation due to shift of $\lambda_D$ by $\pm 3$ cm.
$z_{vtx}$ fit range	3.3%	0	Variation seen using $ z_{vtx}  < 20$ cm, $ z_{vtx}  < 40$ cm.
Input hadron spectrum	0	$(p_T[\text{GeV}/c] - 1) \times 5.0\%$	Spectrum normalized to data, so the only uncertainty here is in the $p_T$ dependence.
Decay normalization	7%	0	Statistical uncertainty in fit to observed free-decay muon yield.
$\sigma_{R_D}$	9.2%	$(p_T[\text{GeV}/c] - 1) \times 5.0\%$	Add all previous rows in quadrature.
$\sigma_{N_I}/N_I$	16.3%	$(p_T[\text{GeV}/c] - 1) \times 5.4\%$	From Table V.
$\sigma_{N_D}/N_D$	18.7%	$(p_T[\text{GeV}/c] - 1) \times 7.4\%$	Add previous two rows in quadrature.

TABLE VII: Sources of systematic error on  $R_P$ , the ratio of punchthrough hadrons to inclusive muon candidates, and  $N_P$ , the absolute yield of punchthrough hadrons.

Error Source	$\sigma/N^{\text{norm}}$	$\sigma/N^{pT}$	Comment
Exponential absorption model	0	32%	Maximum fractional difference between $C^i(p_T)$ for FLUKA and GHEISHA, from Table IV.
$\varepsilon_{\text{scale}}^3$	23%	0	Dominated by ambiguity in the definition of which particles should be reconstructed.
$p$ and $\bar{p}$ contributions	10%	0	Variation with extreme assumptions on the $p$ and $\bar{p}$ nuclear interaction length.
$N_3^{\text{stop}}$ normalization	10%	0	Statistical uncertainty in fit to observed gap 3 exclusive yield.
$\sigma_{R_P}$	27%	32%	Add all previous rows in quadrature.
$\sigma_{N_I}/N_I$	16.3%	$(p_T[\text{GeV}/c] - 1) \times 5.4\%$	From Table V.
$\sigma_{N_P}/N_P$	31.5%	$\approx 32\%$	Add previous two rows in quadrature.

The spectrum also appears to be somewhat harder than the PYTHIA spectrum with the parameters listed in Table VIII.

We scale the charm (only) contribution to the PYTHIA vertex-independent muon  $p_T$  spectrum such that the total spectrum (including the small contributions from open bottom and vector mesons) matches the central values of the measured vertex-independent negative muon spectrum. Only statistical errors are used in the fit. Note, larger systematic errors for the positive muon spectrum preclude a significant measurement for that charge sign. We multiply the scale factor from the fit (2.27) by the PYTHIA value for the charm production cross section,  $d\sigma_{c\bar{c}}/dy|_{y=1.6}^{\text{PYTHIA}}$  (0.107 mb), to obtain  $d\sigma_{c\bar{c}}/dy|_{y=1.6}^{\text{PHENIX}} = 0.243 \pm 0.013(\text{stat.}) \text{ mb}$ .

We distinguish between two different sources of systematic uncertainty on the extraction of the charm cross section: 1) uncertainty in the PYTHIA calculation, and 2) uncertainty in the data, which is largely independent of PYTHIA.

We determined the uncertainty in the data ( $\pm 43\%$ ) by refitting PYTHIA to the data at the minimum and maximum of the  $1\sigma$  systematic error band.

We determined the uncertainty in the PYTHIA calculation with a systematic study in which we varied simulation parameters, extracted the new simulated vertex-independent negative muon spectrum, normalized to the measured spectrum, and extracted  $d\sigma_{c\bar{c}}/dy|_{y=1.6}^{\text{PHENIX}}$  for the modified parameter sets. We varied PDF libraries, the hard scattering scale, the charm quark mass, the

TABLE VIII: Tuned PYTHIA parameters (default settings for this analysis) for determination of charm production cross section central value.

Parameter	Value	Meaning
MSEL	4	Heavy quark production every event (gluon fusion + $q/\bar{q}$ annihilation).
MSTP(32)	4	Hard scattering scale, $Q^2 = \hat{s}$ .
MSTP(33)	1	Use $K$ -factor.
MSTP(52)	2	Use PDF libraries.
MSTP(51)	4046	Select CTEQ5L PDF libraries [76].
MSTP(91)	1	Use Gaussian distribution for intrinsic $k_T$ .
PARP(31)	3.5	$K$ -factor.
PARP(91)	1.5	$\langle k_T \rangle$ (GeV/c).
PARP(93)	5.0	Maximum $k_T$ (GeV/c).
PMAS(4,1)	1.25	$m_c$ (GeV/c).
$D^+/D^0$	0.32	Default charm chemistry ratio.

TABLE IX: Percentage contribution of different sources of vertex-independent muons within our acceptance ( $1 < p_T < 3$  GeV/c and  $1.5 < |\eta| < 1.8$ ), from PYTHIA, with parameters listed in Table VIII (except that MSEL = 2 to generate minimum bias collisions).

Source	Contribution
Open charm	84.6%
Open bottom	6.9%
$\rho, \omega, \phi$	8.1%
Quarkonia	$< 0.1\%$
Drell-Yan	$< 0.1\%$
$\tau$ leptons	0.4%

intrinsic  $k_T$  value, the  $D^+/D^0$  ratio, charm production mechanism selections, and open bottom and vector meson scaling assumptions. The parameter sets used and the results of this study are summarized in Table X.

The PYTHIA charm cross section varies substantially ( $\Delta(d\sigma_{c\bar{c}}/dy)|_{y=1.6}^{PYTHIA} \approx 4$ ) for the chosen parameter sets. However, the extracted experimental charm cross section is relatively stable ( $\Delta(d\sigma_{c\bar{c}}/dy)|_{y=1.6}^{PHENIX} < 0.36$ ). This is due to the fact that the parameter set changes have relatively minor effects on the shape of the predicted vertex-independent muon  $p_T$  spectrum, and we obtain the experimental charm cross section by normalizing the PYTHIA charm cross section by the ratio of the measured and predicted muon  $p_T$  spectra.

One way to visualize this is to plot (see Figure 17) the vertex-independent muon yield in our acceptance *per event in which a  $c\bar{c}$  pair is created* for the different PYTHIA parameter sets. Due to our procedure, parameter sets which give similar vertex-independent muon yields per  $c\bar{c}$  event in the low  $p_T$  region (which dominates the fit) will necessarily give similar values for  $d\sigma_{c\bar{c}}/dy|_{y=1.6}^{PHENIX}$ , whatever the PYTHIA charm cross

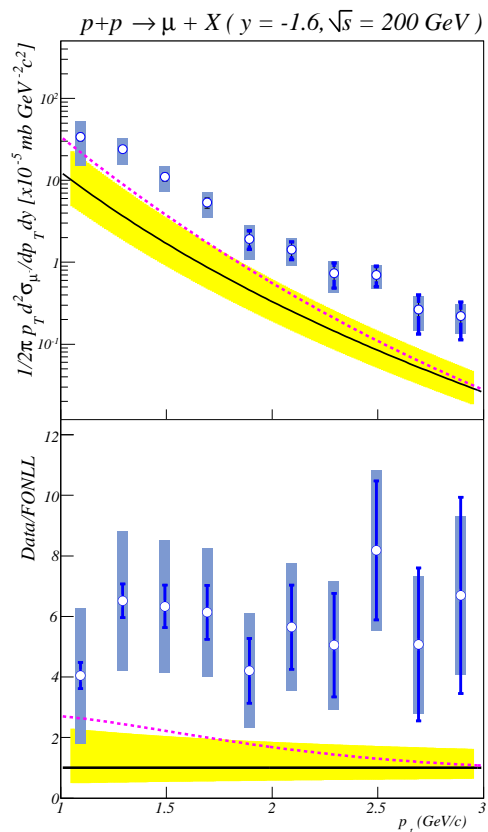


FIG. 16: The top panel shows the measured  $p_T$  spectrum of vertex-independent negative muons from Figure 13, the PYTHIA prediction using settings listed in Table VIII without scaling the charm contribution (dotted line), and a FONLL calculation (solid line with systematic error band) [20, 77]. The bottom panel shows the ratio of the measured spectrum to the FONLL calculation with statistical (error bars) and systematic (bands) uncertainties on the data, as well as the theoretical uncertainty (shaded band around 1). The dashed line shows the PYTHIA/FONLL ratio.

section is.

The largest variation in the predicted muon yield at  $p_T = 1$  GeV/c per  $c\bar{c}$  event is seen for simulations in which the intrinsic  $k_T$  is varied from its default value ( $\langle k_T \rangle = 1.5$  GeV/c) to the value expected from arguments based on Fermi momentum (case 4c,  $\langle k_T \rangle = 0.3$  GeV/c), or to a value which best reproduces the measured spectrum at higher  $p_T$  (case 4d,  $\langle k_T \rangle = 3.0$  GeV/c). These parameter sets also result in the largest variation in  $d\sigma_{c\bar{c}}/dy|_{y=1.6}^{PHENIX}$ , as shown in Table X. We use the cross section values obtained in this pair of simulations to define the systematic uncertainty in our measurement due to the uncertainty in our PYTHIA calculation. This gives us our final answer:  $d\sigma_{c\bar{c}}/dy|_{y=1.6} = 0.243 \pm 0.013(\text{stat.}) \pm 0.105(\text{data syst.})^{+0.049}_{-0.087}(\text{PYTHIA syst.})$  mb.

Figure 18 shows the PHENIX charm rapidity spectrum. The result of this analysis (mirrored about  $y = 0$

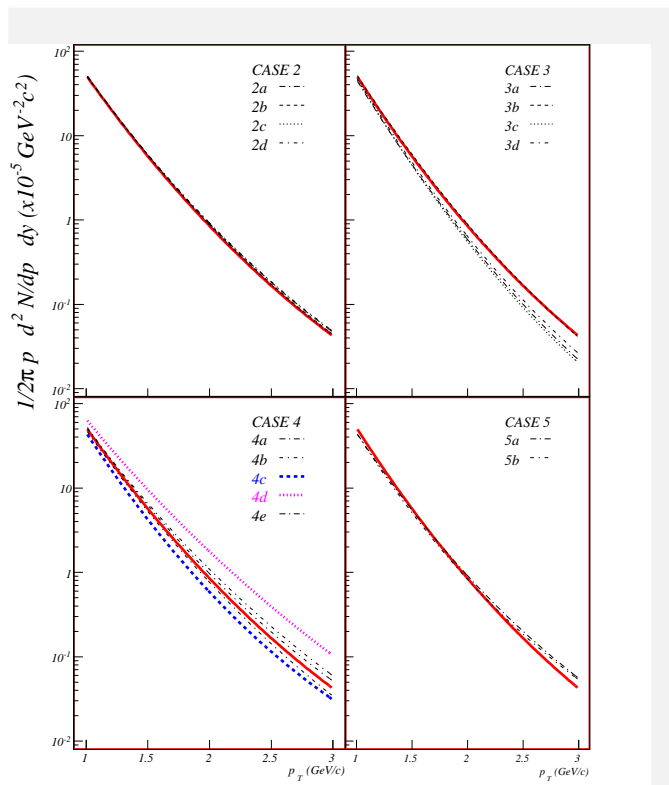


FIG. 17: (Color online) PYTHIA results with different parameter sets for the negative vertex-independent muon  $p_T$  spectrum per event in which a  $c\bar{c}$  pair is created. The solid line in each panel shows the result when using default settings listed in Table VIII. Legends indicate the correspondance between line style and the simulation case label. Parameter sets for each case label are given in Table X.

since this is a symmetric collision system) is plotted along with the result for  $d\sigma_{c\bar{c}}/dy|_{y=0}$  [13]. In order to compare with the data at  $y = 0$  the systematic uncertainty on the data from this analysis is shown as the quadrature sum of the two sources of systematic uncertainty described above (data and PYTHIA). Theoretical curves from PYTHIA (case 1 and case 5a), FONLL [20, 77], and an NLO calculation from Vogt [83] are also displayed.

In the top panel of the figure PYTHIA with the default parameter set (Case 1) is fit to the two PHENIX points with statistical and systematic errors added in quadrature. Other theory curves are normalized so that they are equal at  $y = 0$  in order to allow shape comparisons. As shown in Table X, different PYTHIA parameter sets differ in the predicted ratio  $d\sigma_{c\bar{c}}/dy|_{y=1.6}^{PYTHIA}/d\sigma_{c\bar{c}}/dy|_{y=0}^{PYTHIA}$  by  $> 30\%$ . Unfortunately, current systematic error bars preclude any conclusions about the charm production rapidity shape.

In the bottom panel of the figure the theory curves are unnormalized to allow an absolute comparison. The quoted theoretical uncertainty bands for the FONLL and NLO calculations are also shown. We note that, although our data are above the FONLL prediction, the error bars touch. This is in contrast to the situation for the vertex-independent muon cross section, shown in Figure 16, where the data are significantly

above the prediction. The larger disagreement in the vertex-independent muon cross section is presumably due to different treatment of the fragmentation process in PYTHIA and FONLL [20, 77, 83].

## V. CONCLUSION AND OUTLOOK

We have measured muon production at forward rapidity ( $1.5 \leq |\eta| \leq 1.8$ ), in the range  $1 < p_T < 3$  GeV/c, in  $\sqrt{s} = 200$  GeV  $p + p$  collisions at RHIC. We determined and subtracted the contribution from light hadron sources ( $\pi, K, p$ ) to obtain the vertex-independent muon yield which, for the  $p_T$  range measured in this analysis, and in the absence of new physics, arises dominantly from the decay of  $D$  mesons. We normalized the PYTHIA muon spectrum resulting from the production of charm quarks to obtain the differential cross section for charm production at forward rapidity:  $d\sigma_{c\bar{c}}/dy|_{y=1.6} = 0.243 \pm 0.013(\text{stat.}) \pm 0.105(\text{data syst.})^{+0.049}_{-0.087}(\text{PYTHIA syst.})$  mb. This is compatible with PHENIX charm measurement at  $y = 0$ , although even further above predictions from PYTHIA and FONLL. Large systematic uncertainties in the current measurement preclude statements about the rapidity dependence of the charm cross section.

TABLE X: Results for PYTHIA simulations with different parameter sets used to explore the systematic error on the charm cross section due to model uncertainties. The top of the table details the different parameter sets tested. Unless otherwise noted, parameters are the same as those listed in Table VIII. The bottom of the table gives the results for different simulations: The 1<sup>st</sup> column identifies the simulation; the 2<sup>nd</sup> column gives the total charm production cross section given the chosen PYTHIA parameter set; the 3<sup>rd</sup> column gives the differential charm production cross section at  $y = 1.6$ ; the 4<sup>th</sup> column gives the normalization factor needed to fit the PHENIX data; the 5<sup>th</sup> column gives the differential charm production cross section at  $y = 1.6$  for PHENIX data (the product of the 3<sup>rd</sup> and 4<sup>th</sup> columns); the 6<sup>th</sup> column gives the fractional difference between the results for each simulation compared to the simulation with the default PYTHIA parameter set; the last column gives the ratio  $d\sigma_{c\bar{c}}/dy|_{y=1.6}^{PYTHIA}/d\sigma_{c\bar{c}}/dy|_{y=0}^{PYTHIA}$ .

Case	PYTHIA Settings					
1	Default settings, see Table VIII.					
2a	MSTP(51) = 4032, CTEQ4L PDF libraries [78].					
2b	MSTP(51) = 5005, GRV94LO PDF libraries [79].					
2c	MSTP(51) = 5012, GRV98LO PDF libraries [80].					
2d	MSTP(51) = 3072, MRST (c-g) PDF libraries [81].					
3a	MSTP(32) = 1, $Q^2 = 2\hat{s}\hat{t}\hat{u}/(\hat{s}^2 + \hat{t}^2 + \hat{u}^2)$ .					
3b	MSTP(32) = 2, $Q^2 = p_T^2 + (m_3^2 + m_4^2)/2$ .					
3c	MSTP(32) = 3, $Q^2 = \min(-\hat{t}, -\hat{u})$ .					
3d	MSTP(32) = 5, $Q^2 = -\hat{t}$ .					
4a	PMAS(4, 1) = $m_c = 1.15$ GeV/c.					
4b	PMAS(4, 1) = $m_c = 1.35$ GeV/c.					
4c	PARP(91) = $\langle k_T \rangle = 0.3$ GeV/c.					
4d	PARP(91) = $\langle k_T \rangle = 3.0$ GeV/c.					
4e	MSTP(68) = 2, Maximum virtuality scale and matrix element matching scheme. PARP(67) = 4, Multiplicative factor applied to hard scattering scale.					
5a	PARP(31) = $K$ -factor = 1, MSEL = 1, Hard scattering enabled.					
5b	PARP(31) = $K$ -factor = 1, MSEL = 1, Hard scattering enabled, All other parameters untuned.					
6	$D^+/D^0 = 0.45$ [82].					
7	Open bottom and vector mesons scale with charm.					
Case	$\sigma_{c\bar{c}}^{PYTHIA}$ (mb)	$d\sigma_{c\bar{c}}/dy _{y=1.6}^{PYTHIA}$ (mb)	Normalization to Data	$d\sigma_{c\bar{c}}/dy _{y=1.6}^{PHENIX}$ (mb)	$\Delta d\sigma_{c\bar{c}}/dy _{y=1.6}^{PHENIX}$ (%)	$d\sigma_{c\bar{c}}/dy _{y=1.6}^{PYTHIA}/$ $d\sigma_{c\bar{c}}/dy _{y=0}^{PYTHIA}$
1	0.658	0.107	2.27	0.243	–	0.67
2a	0.691	0.111	2.10	0.232	-4.5	0.69
2b	0.698	0.112	2.09	0.233	-3.9	0.71
2c	0.669	0.109	2.18	0.238	-1.7	0.73
2d	0.551	0.088	2.67	0.236	-2.9	0.71
3a	1.520	0.243	1.12	0.271	11.8	0.84
3b	0.863	0.139	1.63	0.226	-6.7	0.71
3c	1.501	0.242	1.11	0.267	10.2	0.84
3d	1.104	0.178	1.45	0.258	6.4	0.78
4a	0.905	0.145	1.73	0.252	3.7	0.67
4b	0.487	0.078	2.91	0.226	-6.7	0.64
4c	0.658	0.104	2.81	0.292	20.4	0.66
4d	0.658	0.104	1.50	0.156	-35.8	0.63
4e	0.658	0.106	2.09	0.220	-9.2	0.63
5a	0.435	0.068	3.91	0.266	9.4	0.80
5b	0.385	0.058	4.67	0.271	11.7	0.79
6	0.658	0.107	2.38	0.255	5.0	0.67
7	0.658	0.107	2.20	0.236	-2.9	0.67

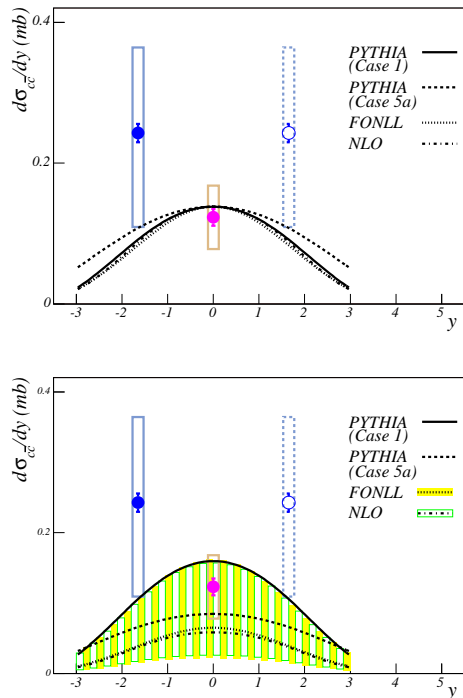


FIG. 18: (Color online) Comparisons of measured charm rapidity distributions,  $d\sigma_{c\bar{c}}/dy$  vs.  $y$ , to theoretical predictions. Data points at  $y = \pm 1.6$  are from this analysis (the point at  $y = 1.6$  is reflected through  $y = 0$ ). The point at  $y = 0$  is the PHENIX measurement of charm through semileptonic decay to electrons [13]. Error bars on the data points indicate statistical uncertainties and boxes indicate systematic uncertainties. The top panel shows rapidity spectra from two PYTHIA parameter sets (see Table X for details), FONLL [20, 77], and an NLO calculation [83]. The PYTHIA curve with the default parameter set (Case 1) was fit to the two PHENIX data points with statistical and systematic errors added in quadrature. All other theory curves were normalized so that they are equal at  $y = 0$  to allow shape comparisons. The bottom panel shows the theory curves unnormalized. Theoretical uncertainties associated with the FONLL and NLO calculations are indicated with shaded bands.

The systematic uncertainty in the data is dominated by uncertainty on the determination of the fractional contribution of decay muons. This will be improved with higher statistics data sets (already collected) which will allow better measurements of the  $z_{vtx}$  dependence of particle production. Final results for identified particle  $p_T$  distributions in  $p + p$  collisions by BRAHMS will also be invaluable for improving the input to our hadron generator. The systematic uncertainty in PYTHIA is dominated by differences observed when the intrinsic  $\langle k_T \rangle$  is varied. In order to reduce this uncertainty we need to reduce the allowed parameter space by improving the measurement of the high  $p_T$  portion of the vertex-independent muon spectrum, where the error is dominated by the uncertainty in the yield of punchthrough hadrons. Data sets (already collected) with higher statis-

tics, and with hadrons stopping in MuID gap 2, will allow a completely data-driven approach to the calculation of the punchthrough yield. This will eliminate the reliance on hadronic interaction simulation packages, differences in which are the largest source of systematic error at high  $p_T$ . Analogous measurements are also being carried out for  $d + Au$ ,  $Cu + Cu$ , and  $Au + Au$  [84] collisions at  $\sqrt{s_{NN}} = 200$  GeV. These will allow determination of the magnitude of nuclear modification effects on charm production at forward rapidity.

## VI. ACKNOWLEDGEMENTS

We thank the staff of the Collider-Accelerator and Physics Departments at Brookhaven National Laboratory and the staff of the other PHENIX participating institutions for their vital contributions. We acknowledge support from the Department of Energy, Office of Science, Nuclear Physics Division, the National Science Foundation, Abilene Christian University Research Council, Research Foundation of SUNY, and Dean of the College of Arts and Sciences, Vanderbilt University (U.S.A), Ministry of Education, Culture, Sports, Science, and Technology and the Japan Society for the Promotion of Science (Japan), Conselho Nacional de Desenvolvimento Científico e Tecnológico and Fundação de Amparo à Pesquisa do Estado de São Paulo (Brazil), Natural Science Foundation of China (People's Republic of China), Centre National de la Recherche Scientifique, Commissariat à l'Énergie Atomique, Institut National de Physique Nucléaire et de Physique des Particules, and Institut National de Physique Nucléaire et de Physique des Particules, (France), Bundesministerium für Bildung und Forschung, Deutscher Akademischer Austausch Dienst, and Alexander von Humboldt Stiftung (Germany), Hungarian National Science Fund, OTKA (Hungary), Department of Atomic Energy and Department of Science and Technology (India), Israel Science Foundation (Israel), Korea Research Foundation and Korea Science and Engineering Foundation (Korea), Russian Ministry of Industry, Science and Technologies, Russian Academy of Science, Russian Ministry of Atomic Energy (Russia), VR and the Wallenberg Foundation (Sweden), the U.S. Civilian Research and Development Foundation for the Independent States of the Former Soviet Union, the US-Hungarian NSF-OTKA-MTA, the US-Israel Binational Science Foundation, and the 5th European Union TMR Marie-Curie Programme.

- 
- [1] B. Abbott et al. (D0), Phys. Rev. Lett **84**, 5478 (2000), hep-ex/9907029.
- [2] D. Acosta et al. (CDF), Phys. Rev. **D71**, 032001 (2005), hep-ex/0412071.
- [3] M. Cacciari (2004), hep-ph/0407187.
- [4] M. Cacciari and M. Greco and P. Nason, JHEP **9805**, 007 (1998), hep-ph/9803400.
- [5] M.L. Mangano (2004), hep-ph/0411020.
- [6] D. Acosta et al. (CDF), Phys. Rev. Lett. **91**, 241804 (2003), hep-ex/0307080.
- [7] K. Adcox et al. (PHENIX), Phys. Rev. Lett. **88**, 192303 (2002), nucl-ex/0202002.
- [8] S.S. Adler et al. (PHENIX), Phys. Rev. Lett. **94**, 082301 (2005), nucl-ex/0409028.
- [9] S.S. Adler et al. (PHENIX), Phys. Rev. Lett. **96**, 032001 (2006), hep-ex/0508034.
- [10] S. Kelly, for the PHENIX Collaboration, J. Phys. **G30**, S1189 (2004), nucl-ex/0403057.
- [11] S.S. Adler et al. (PHENIX), Phys. Rev. Lett. **96**, 032301 (2006), nucl-ex/0510047.
- [12] S. Butsyk, for the PHENIX Collaboration, Proceedings of Quark Matter 2005, to be published in Nucl. Phys. **A** (2005), nucl-ex/0510010.
- [13] A. Adare et al. (PHENIX) (2006), hep-ex/0609010.
- [14] S.S. Adler et al. (PHENIX), Phys. Rev. **C72**, 024901 (2005), nucl-ex/052009.
- [15] S. Sakai, for the PHENIX Collaboration, Proceedings of Quark Matter 2005, to be published in Nucl. Phys. **A** (2005), nucl-ex/0510027.
- [16] A. Adare et al. (PHENIX), to be published (2006).
- [17] J. Adams et al. (STAR), Phys. Rev. Lett **94**, 062301 (2005), nucl-ex/0407006.
- [18] B.I. Abelev et al. (STAR) (2006), nucl-ex/0607012.
- [19] T. Sjöstrand et al., Comput. Phys. Commun. **135**, 238 (2001), hep-ph/0010017.
- [20] M. Cacciari, P. Nason, and R. Vogt, Phys. Rev. Lett. **95**, 122001 (2005), hep-ph/0502203.
- [21] M.L. Mangano, Nucl. Phys. **B405**, 507 (1993).
- [22] R. Vogt (2002), hep-ph/0203151.
- [23] R. Vogt, Int. J. Mod. Phys. **E12**, 211 (2003), hep-ph/0111271.
- [24] W. Cassing, E. Bratkovskaya, and A. Sibirtsev, Nucl. Phys. **A691**, 753 (2001), nucl-th/0010071.
- [25] E.L. Bratkovskaya, W. Cassing, and H. Stöcker, Phys. Rev. **C67**, 054905 (2003), nucl-th/0301083.
- [26] C.-Y. Wong, *Introduction to High-Energy Heavy-Ion Collisions* (World Scientific Publishing Co. Pte. Ltd., 1994), p. 251.
- [27] M.B. Johnson et al. (E772), Phys. Rev. Lett. **86**, 4483 (2001), hep-ex/0010051.
- [28] G.T. Bodwin, S.J. Brodsky, and G.P. Lepage, Phys. Rev. Lett. **47**, 1799 (1981).
- [29] G.T. Bodwin, Phys. Rev. **D31**, 2616 (1985).
- [30] G.T. Bodwin, S.J. Brodsky, and G.P. Lepage, Phys. Rev. **D39**, 3287 (1989).
- [31] B.Z. Kopeliovich and F. Niedermayer, Tech. Rep. E2-84-834, Dubna (1984), URL <http://ccdb3fs.kek.jp/cgi-bin/img/allpdf?198504113>.
- [32] S. Gavin and J. Milana, Phys. Rev. Lett. **68**, 1834 (1992).
- [33] V. Guzey, M. Strikman, and W. Vogelsang, Phys. Lett. **B603**, 173 (2004), hep-ph/0407201.
- [34] Y.L. Dokshitzer and D.E. Kharzeev, Phys. Lett. **B519**, 199 (2001), hep-ph/0106202.
- [35] L. McLerran and R. Venugopalan, Phys. Rev. **D49**, 2233 (1994).
- [36] L. McLerran and R. Venugopalan, Phys. Rev. **D49**, 3352 (1994).
- [37] J. Ashman et al. (EMC), Phys. Lett. **B202**, 603 (1988).
- [38] R. Baier, D. Schiff, and B. Zakharov, Ann. Rev. Nucl. Part. Sci. **50**, 37 (2000), hep-ph/0002198.
- [39] J.A. Appel, Ann. Rev. Nucl. Part. Sci. **42**, 367 (1992).
- [40] B. Müller and X.N. Wang, Phys. Rev. Lett. **68**, 2437 (1992).
- [41] T. Matsui and H. Satz, Phys. Lett. **B178**, 416 (1986).
- [42] H. Satz, J. Phys. **G32**, R25 (2006), hep-ph/0512217.
- [43] R.L. Thews and M.L. Mangano, Phys. Rev. **C73**, 014904 (2006), nucl-th/0505055.
- [44] L. Grandchamp, R. Rapp and G.E. Brown, Phys. Rev. Lett. **92**, 212301 (2004), hep-ph/0306077.
- [45] A. Andronic et al., Phys. Lett. **B571**, 36 (2003), nucl-th/0303036.
- [46] A.P. Kostyuk et al., Phys. Rev. **C68**, 041902(R) (2003), hep-ph/0305277.
- [47] S.S. Adler et al. (PHENIX), Phys. Rev. Lett. **94**, 082302 (2005), nucl-ex/0411054.
- [48] I. Arsene et al. (BRAHMS), Phys. Rev. Lett **94**, 032301 (2005), nucl-ex/0401025.
- [49] I. Arsene et al. (BRAHMS), Phys. Rev. Lett **93**, 242303 (2004), nucl-ex/0403005.
- [50] J. Adams et al. (STAR) (2006), nucl-ex/0602011.
- [51] S.S. Adler et al. (PHENIX), Phys. Rev. Lett. **92**, 051802 (2004), hep-ex/0307019.
- [52] S.S. Adler et al. (PHENIX), Phys. Rev. Lett. **96**, 012304 (2006), nucl-ex/0507032.
- [53] H. Pereira Da Costa, for the PHENIX Collaboration, Proceedings of Quark Matter 2005, to be published in Nucl. Phys. **A** (2005), nucl-ex/0510051.
- [54] K. Adcox et al. (PHENIX), Nucl. Instrum. Methods **A499**, 469 (2003).
- [55] S.S. Adler et al. (PHENIX), Nucl. Instrum. Methods **A499**, 560 (2003).
- [56] S.S. Adler et al. (PHENIX), Nucl. Instrum. Methods **A499**, 593 (2003).
- [57] M. Allen et al. (PHENIX), Nucl. Instrum. Methods **A499**, 549 (2003).
- [58] H. Akikawa et al. (PHENIX), Nucl. Instrum. Methods **A499**, 537 (2003).
- [59] S.H. Aronson et al. (PHENIX), Nucl. Instrum. Methods **A499**, 480 (2003).
- [60] S.S. Adler et al. (PHENIX), Phys. Rev. Lett. **91**, 241803 (2003), hep-ex/0304038.
- [61] *GEANT 3.2.1 Manual* (1994), CERN W5013, URL <http://wwwasdoc.web.cern.ch/wwwasdoc/pdfdir/geant.pdf>.
- [62] V.L. Highland, Nucl. Instrum. Methods **129**, 497 (1975).
- [63] V.L. Highland, Nucl. Instrum. Methods **161**, 171 (1979).
- [64] G.R. Lynch and O.I. Dahl, Nucl. Instrum. Methods **B58**, 6 (1991).
- [65] S.S. Adler et al. (PHENIX), to be submitted to Phys. Rev. **D**.
- [66] V. Ryabov, for the PHENIX Collaboration, Proceedings of Quark Matter 2005, to be published in Nucl. Phys. **A** (2005), hep-ex/0510017.



- [67] S. Eidelman et al., Phys. Lett. **B592**, 1 (2004), URL <http://pdg.lbl.gov>.
- [68] A. Fassò et al., in *Proceedings of the MonteCarlo 2000 Conference, Lisbon, October 23-26, 2000*, edited by A. Kling et al. (Springer-Verlag, Berlin, 2001), p. 955, URL <http://www.fluka.org>.
- [69] H.S. Fesefeldt, Tech. Rep. PITHA 85/02, Aachen (1985).
- [70] E.W. Cornell et al., Nucl. Instrum. Methods **A350**, 150 (1994).
- [71] G.A. Alves et al. (E769), Phys. Rev. Lett. **77**, 2388 (1996).
- [72] F.W. Büsser et al., Nucl. Phys. **B113**, 189 (1976).
- [73] P. Perez et al., Phys. Lett. **B112**, 260 (1982).
- [74] M. Basile et al., Nuovo Cimento Soc. Ital. Fis. **A65**, 421 (1981).
- [75] T. Sjöstrand et al. (2001), hep-ph/0108264.
- [76] H.L. Lai et al. (CTEQ), Eur. Phys. J **C12**, 375 (2000), hep-ph/9903282.
- [77] M. Cacciari, private communication.
- [78] H.L. Lai et al. (CTEQ), Phys. Rev. **D55**, 1280 (1997), hep-ph/9606399.
- [79] M. Gluck, E. Reya, and R. Vogt, Z. Phys. **C67**, 433 (1995).
- [80] M. Gluck, E. Reya, and R. Vogt, Eur. Phys. J. **C5**, 461 (1998), hep-ph/9806404.
- [81] A.D. Martin et al., Eur. Phys. J. **C23**, 73 (2002), hep-ph/0110215.
- [82] A. Tai, for the STAR Collaboration, J. Phys. **G30**, S809 (2004), nucl-ex/0404029.
- [83] R. Vogt, private communication.
- [84] X.R. Wang, for the PHENIX Collaboration, Proceedings of Particles and Nuclei International Conference (PANIC) 2005, to be published in J. Phys. **G** (2006), hep-ex/0603051.